

Giant squid-hidden canard: the 3D geometry of the Hodgkin–Huxley model

Jonathan Rubin · Martin Wechselberger

Received: 8 November 2006 / Accepted: 11 March 2007 / Published online: 26 April 2007
© Springer-Verlag 2007

Abstract This work is motivated by the observation of remarkably slow firing in the uncoupled Hodgkin–Huxley model, depending on parameters τ_h, τ_n that scale the rates of change of the gating variables. After reducing the model to an appropriate nondimensionalized form featuring one fast and two slow variables, we use geometric singular perturbation theory to analyze the model's dynamics under systematic variation of the parameters τ_h, τ_n , and applied current I . As expected, we find that for fixed (τ_h, τ_n) , the model undergoes a transition from excitable, with a stable resting equilibrium state, to oscillatory, featuring classical relaxation oscillations, as I increases. Interestingly, mixed-mode oscillations (MMO's), featuring slow action potential generation, arise for an intermediate range of I values, if τ_h or τ_n is sufficiently large. Our analysis explains in detail the geometric mechanisms underlying these results, which depend crucially on the presence of two slow variables, and allows for the quantitative estimation of transitional parameter values, in the singular limit. In particular, we show that the sub-threshold oscillations in the observed MMO patterns arise through a generalized canard phenomenon. Finally, we discuss the relation of results obtained in the singular limit to the behavior observed away from, but near, this limit.

1 Introduction

The Hodgkin–Huxley (HH) model (Hodgkin and Huxley 1952) for the action potential of the space-clamped squid giant axon is defined by the following 4D vector field:

$$\begin{aligned} C \frac{dV}{dt} &= I - I_{Na} - I_K - I_L \\ \frac{dm}{dt} &= \phi[\alpha_m(V)(1 - m) - \beta_m(V)m] \\ \frac{dh}{dt} &= \phi[\alpha_h(V)(1 - h) - \beta_h(V)h] \\ \frac{dn}{dt} &= \phi[\alpha_n(V)(1 - n) - \beta_n(V)n]. \end{aligned} \quad (1.1)$$

We use modern conventions such that the spikes of action potentials are positive, and the voltage \tilde{V} of the original HH model (Hodgkin and Huxley 1952) is shifted relative to the voltage V of this model by $\tilde{V} = (V + 65)$.

The first equation is obtained by applying Kirchhoff's law to the space-clamped neuron, i.e. the transmembrane current is equal to the sum of intrinsic currents. C is the capacitance density in $\mu F/cm^2$, V is the membrane potential in mV and t is the time in ms . The ionic currents on the right hand side are given by

$$\begin{aligned} I_{Na} &= g_{Na}m^3h(V - E_{Na}), \quad I_K = g_Kn^4(V - E_K), \\ I_L &= g_L(V - E_L) \end{aligned} \quad (1.2)$$

with a fast sodium current I_{Na} , a delayed rectifier potassium current I_K and a small leak current I_L , which consists mainly of chloride current. The current densities I_x ($x = Na, K, L$) are measured in $\mu A/cm^2$ and the conductance densities g_x in mS/cm^2 . The parameter I represents current injected into the space-clamped axon and E_x are the equilibrium potentials or Nernst potentials in mV for the various ions. The parameters are given by

J. Rubin (✉)
Department of Mathematics
and Center for the Neural Basis of Cognition,
University of Pittsburgh, Pittsburgh, PA, USA
e-mail: rubin@math.pitt.edu

M. Wechselberger
School of Mathematics and Statistics,
University of Sydney,
Sydney, NSW, Australia

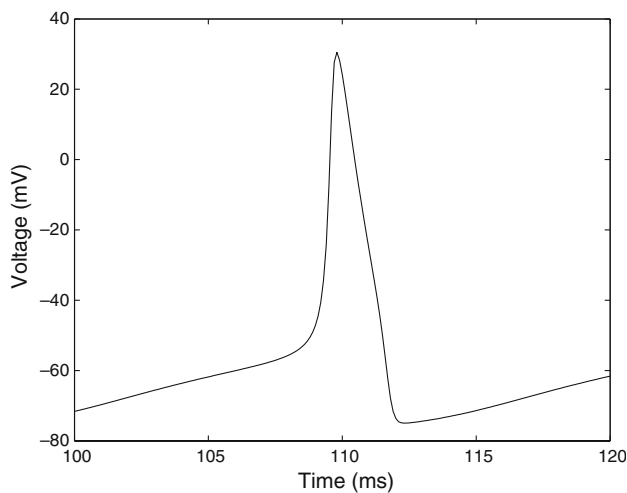


Fig. 1 Action potential generated by the HH model with applied current $I = 9.6$ at 6.3°C

$$\begin{aligned} g_{Na} &= 120, \quad g_K = 36, \quad g_L = 0.3, \\ E_{Na} &= 50, \quad E_K = -77, \quad E_L = -54.4, \\ C &= 1. \end{aligned} \quad (1.3)$$

The conductances of the ionic currents are regulated by voltage dependent activation and inactivation variables called gating variables. Their dynamics are described by the other three equations in (1.1), where m denotes the activation of the sodium current, h the inactivation of the sodium current, and n the activation of the potassium current.

Each of these equations features a temperature scaling factor $\phi = (Q_{10})^{(T-T_0)/10}$, where Q_{10} is a constant, T is temperature, and $T_0 = 6.3$, both in degrees celsius. The gating variables are dimensionless with their ranges in the interval $[0,1]$.

The specific functions α_z and β_z ($z = m, h, n$) on the right hand sides are, in units of $(ms)^{-1}$,

$$\begin{aligned} \alpha_m(V) &= \frac{(V + 40)/10}{1 - \exp(-(V + 40)/10)}, \\ \beta_m(V) &= 4 \exp(-(V + 65)/18) \\ \alpha_h(V) &= 0.07 \exp(-(V + 65)/20), \\ \beta_h(V) &= 1 / (1 + \exp(-(V + 35)/10)) \\ \alpha_n(V) &= \frac{(V + 55)/100}{1 - \exp(-(V + 55)/10)}, \\ \beta_n(V) &= 0.125 \exp(-(V + 65)/80). \end{aligned} \quad (1.4)$$

Figure 1 shows an action potential at 6.3°C simulated by the HH model, which is in good agreement with measured action potential data of the squid giant axon (Hodgkin and Huxley 1952).

FitzHugh (FitzHugh 1960) has given an elegant qualitative description of the HH equations, based on the fact that the model variables (V, m) have fast kinetics, while (h, n) have slow kinetics. This allows the full 4D phase space to be broken into smaller pieces (2D subspaces) by fixing the slow variables and considering the behaviour of the model as a function of the fast variables. This idea provides a useful way to study the process of excitation (see also Nagumo et al. 1962).

Based on FitzHugh's analysis, another model reduction was proposed (see e.g. Rinzel 1985), which keeps the slow-fast structure of the equations, but reduces the system to a 2D model. The reductions are based on the following observations:

- The activation of sodium channels m is (very) fast. Therefore m will reach its equilibrium almost instantaneously and $m = \alpha_m(V)/(\alpha_m(V) + \beta_m(V)) =: m_\infty(V)$ can be assumed.
- As FitzHugh already noticed (FitzHugh 1960), in the course of an action potential there appears to be an approximately linear relation between h and n . Thus n can be approximated by a linear function $n = n(h)$.

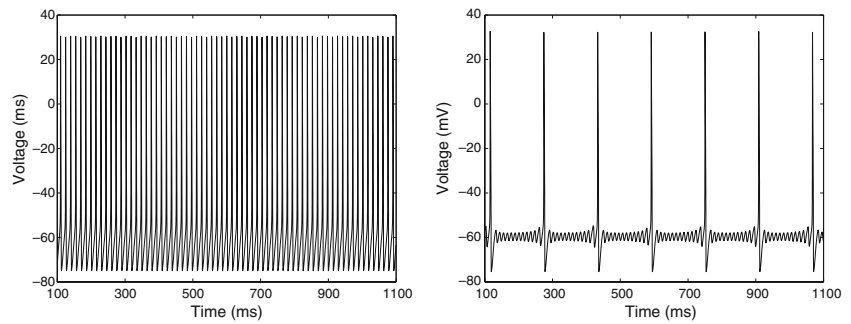
The first reduction can be mathematically justified by a center manifold reduction (see Theorem 1), which reduces the HH model to a 1 fast, 2 slow variable model. The second reduction is a purely empirical observation and has no mathematical justification. There is no *a priori* argument as to why the nonlinear variables (n, h) should have a linear relation. Nonetheless, the reduced HH model resulting from applying this relationship can describe the action potential (Fig. 1) very well and can be analyzed in the corresponding 2D phase space.

It has become conventional wisdom that the qualitative properties of the Hodgkin–Huxley model can be reduced to a 2D flow such as that described by Rinzel (1985). But these reductions do not capture the full dynamics of the full HH model. Rinzel and Miller (1980) as well as Guckenheimer and Oliva (2002) have given evidence for chaos in the HH model. This clearly points out that a rigorous reduction to a 2D model is not possible, as chaos requires models with phase spaces of at least three dimensions.

Another interesting observation was made in a variation of the HH model by Doi et al. (Doi and Kumagai 2001, 2005; Doi et al. 2001, 2004), who replaced ϕ in (1.1) with three independent time constants τ_m, τ_h, τ_n :

$$\begin{aligned} C \frac{dV}{dt} &= I - g_{Na} m^3 h (V - E_{Na}) - g_K n^4 (V - E_K) \\ &\quad - g_L (V - E_L) \\ \frac{dm}{dt} &= \frac{1}{\tau_m} (\alpha_m(V)(1 - m) - \beta_m(V)m) \end{aligned} \quad (1.5)$$

Fig. 2 Simulation of modified HH model with applied current $I = 9.6$. *Left* $\tau_h = 1$ yields a firing frequency of approximately 70 Hz. *Right* $\tau_h = 2$ yields a firing frequency of approximately 7 Hz



$$\begin{aligned} \frac{dh}{dt} &= \frac{1}{\tau_h}(\alpha_h(V)(1 - h) - \beta_h(V)h) \\ \frac{dn}{dt} &= \frac{1}{\tau_n}(\alpha_n(V)(1 - n) - \beta_n(V)n), \end{aligned}$$

where $\tau_m = \tau_h = \tau_n = 1$ corresponds to the classical HH model at 6.3°C. In their work they observed a dramatic slowing of the firing rate when they increased either τ_h or τ_n ten fold. Actually, such a big change in the time constants is not needed to observe this behaviour. If e.g. τ_h is changed from 1 to 2, then the firing rate of action potentials due to applied current $I = 9.6$ slows down dramatically, from approximately 70 to 7 Hz (see Fig. 2). This represents a ten fold decrease in firing rate, although the time constant was just increased two fold. Note the sub-threshold oscillations in the interspike intervals for $\tau_h = 2$, which do not exist for $\tau_h = 1$. Furthermore, Doi et al. (Doi and Kumagai 2001, 2005; Doi et al. 2001, 2004) also observed chaotic behaviour within this modified model (not shown here), which indicates again that the classical 2D reduction is not appropriate to capture the full dynamics of the classical HH model.

An interesting observation is that modifying the speed of activation and inactivation of the ion channels leaves the monotonic steady-state current-voltage relation of the model neuron unchanged. Therefore the modified HH model is still classified as a ‘Type II’ neuron, as is the classical HH model (Rinzel and Ermentrout 1989). Previously, it had been believed that slow firing rates in single neuron models could be achieved only in ‘Type I’ neurons, which have an N-shaped current voltage relation, as found for neurons with A-type potassium channels. The wide range of firing rates seen there is due to a homoclinic bifurcation in the 2D phase space, which may, for example, arise as a reduction from a saddle-node bifurcation of fixed points on an invariant circle in a higher-dimensional space. The 3D analysis we present here explains a dynamic mechanism by which ‘Type II’ model neurons can also have a wide range of firing rates. The main question we address is the following: *How does a slow firing rate emerge from the geometry of the HH model?*

A similar observation of significant slowing of firing rates, as in Fig. 2, has been made by Drover et al. (Drover et al. 2004;

Rubin 2005) in a network of (Type II) HH model neurons coupled with excitatory synapses. This network synchronizes very quickly after synaptic excitation is activated and the firing rate of the network slows down dramatically, compared to the single neuron firing rate with constant current injection. The analysis of this network can be reduced to a 3D model. The key to understanding the observed activity is the so called ‘canard phenomenon’ (Benoit 1983; Szmolyan and Wechselberger 2001), which traps the solution for a significant amount of time near the expected action potential threshold before it can fire again. Wechselberger (2005a) has shown that the extreme delay is due to canards of folded node type (Szmolyan and Wechselberger 2001). The ‘vortex structure’ described in Drover et al. (2004) can be rigorously understood in terms of invariant manifolds analysed in Wechselberger (2005a), which form a multi-layered trapping region.

The solutions with significant delays that we have described above consist of a certain number of subthreshold oscillations combined with a relaxation oscillation type action potential, as shown in Fig. 2 for $\tau_h = 2$. Such solutions are called ‘mixed-mode-oscillations’ (MMO’s), and their relation to the canard phenomenon was first demonstrated by Milik et al. (1998). A more detailed analysis of MMO’s and generalization of the canard phenomenon was done by Brøns et al. (2006).

In this paper, we apply geometric singular perturbation techniques (Szmolyan and Wechselberger 2001, 2004; Wechselberger 2005a; Brøns et al. 2006) suitable for the analysis of the single HH neuron carefully, explain how a significant slowing of the firing rate may occur, and explain a mechanism through which complex oscillatory patterns may arise in this system.

The outline is as follows: In Sect. 2 we reduce the HH model to a 3D model that captures all the qualitative features observed in the full model. In Sect. 3 we give an overview of results on relaxation oscillations and MMO’s in general, using results from geometric singular perturbation theory. In Sect. 4 we apply these results to the reduced 3D HH model. This enables us to explain the mechanism underlying the

observed oscillatory phenomena and to predict what forms of solutions will arise as τ_h , τ_n , and I are varied. Finally, in Sect. 5 we conclude with a discussion.

2 HH model reduction

We will apply geometric singular perturbation techniques for the analysis of the HH equation, formulated to include the modification proposed by Doi et al. (Doi and Kumagai 2001, 2005; Doi et al. 2001, 2004):

$$\begin{aligned}
 C \frac{dV}{dt} &= I - g_{na}m^3h(V - E_{Na}) - g_kn^4(V - E_K) \\
 &\quad - g_l(V - E_L) \\
 \frac{dm}{dt} &= \frac{1}{\tau_m \hat{\tau}_m(V)}(m_\infty(V) - m) \\
 \frac{dh}{dt} &= \frac{1}{\tau_h \hat{\tau}_h(V)}(h_\infty(V) - h) \\
 \frac{dn}{dt} &= \frac{1}{\tau_n \hat{\tau}_n(V)}(n_\infty(V) - n)
 \end{aligned}
 \tag{2.6}$$

where $\hat{\tau}_x(V)$ (in ms) and $x_\infty(V)$ (dimensionless), with $x = m, h, n$, are defined as follows:

$$\begin{aligned}
 \hat{\tau}_x(V) &= \frac{1}{\alpha_x(V) + \beta_x(V)}, \\
 x_\infty(V) &= \frac{\alpha_x(V)}{\alpha_x(V) + \beta_x(V)}.
 \end{aligned}
 \tag{2.7}$$

2.1 Dimensionless version of the HH model

As a starting point we nondimensionalize system (2.6) and identify a small perturbation parameter ε such that we can apply singular perturbation techniques. The following table shows the units of the variables and parameters in system (2.6):

variable	units	parameter	units
V	mV	E_x	mV
m	1	g_x	mS/cm^2
h	1	C	$\mu F/cm^2$
n	1	I	$\mu A/cm^2$
t	ms	τ_x	1

To make the variables (V, t) dimensionless, we have to identify a typical voltage scale k_v and a typical time scale k_t , and define new dimensionless variables (v, τ) such that

$$V = k_v \cdot v, \quad t = k_t \cdot \tau.
 \tag{2.8}$$

Using this transformation, the dimensionless HH system is then given by

$$\begin{aligned}
 \frac{dv}{d\tau} &= \frac{k_t \cdot g}{C} [\bar{I} - \bar{g}_{na}m^3h(v - \bar{E}_{Na}) - \bar{g}_kn^4(v - \bar{E}_K) \\
 &\quad - \bar{g}_l(v - \bar{E}_L)] \\
 \frac{dm}{d\tau} &= \frac{k_t}{\tau_m \hat{\tau}_m(v)}(m_\infty(v) - m) \\
 \frac{dh}{d\tau} &= \frac{k_t}{\tau_h \hat{\tau}_h(v)}(h_\infty(v) - h) \\
 \frac{dn}{d\tau} &= \frac{k_t}{\tau_n \hat{\tau}_n(v)}(n_\infty(v) - n)
 \end{aligned}
 \tag{2.9}$$

with dimensionless parameters $\bar{E}_x = E_x/k_v$, $\bar{g}_x = g_x/g$ and $\bar{I} = I/(k_v \cdot g)$, where g is a reference conductance, chosen as $g = g_{na}$, since this is the maximum conductance in this problem. The Nernst potentials E_x set a natural range for the observed action potentials as $E_K \leq V \leq E_{Na}$. Therefore the maximum variation of the membrane potential is 127 mV in our problem, and we choose $k_v = 100$ mV as a typical scale for the potential V . Note that under the choice $g = g_{na}$, all terms in the square bracket of the right hand side of the first equation in (2.9) are bounded (in absolute values) by one. Therefore the characteristic scale of this right hand side is given by $(k_t \cdot g_{Na})/C$.

Next, let us check the right hand sides of the gating equations in (2.9). We have $0 \leq x \leq 1, 0 \leq x_\infty(v) \leq 1$ and therefore $|x_\infty(v) - x| \leq 1$. The only differences in the orders of magnitude of the gating equations may arise from the functions $\hat{\tau}_x(v)$. The functions $\hat{\tau}_x(v)$ are given in ms and therefore include characteristic timescales. Recall from (2.7) that

$$1/\hat{\tau}_x(v) = \alpha_x(v) + \beta_x(v).
 \tag{2.10}$$

Figure 3 shows a plot of the functions $1/\hat{\tau}_x(v)$ over the physiological range $v \in [-0.77, 0.5]$. This figure shows that $\max_{v \in [-0.77, 0.5]}(1/\hat{\tau}_m(v))$ is of an order of magnitude bigger than $1/\hat{\tau}_h(v)$ and $1/\hat{\tau}_n(v)$, which are of comparable size. We define $1/\hat{\tau}_x(v) = \hat{T}_x/\hat{t}_x(v)$ where $\hat{T}_x = \max_{v \in [-0.77, 0.5]}(1/\hat{\tau}_x(v))$. Note that \hat{T}_x has dimension $(ms)^{-1}$ while $\hat{t}_x(v)$ is now dimensionless and $1/\hat{t}_x(v) \leq 1$ for $v \in [-0.77, 0.5]$.

The values of the scaling factors are approximately $\hat{T}_m \approx 10 (ms)^{-1}$ while $\hat{T}_h \approx \hat{T}_n \approx 1 (ms)^{-1}$ (see Fig. 3). From (2.9), we obtain the following system

$$\begin{aligned}
 \frac{C}{k_t \cdot g_{Na}} \frac{dv}{d\tau} &= [\bar{I} - \bar{g}_{na}m^3h(v - \bar{E}_{Na}) \\
 &\quad - \bar{g}_kn^4(v - \bar{E}_K) - \bar{g}_l(v - \bar{E}_L)] \\
 \frac{1}{\hat{T}_m k_t} \frac{dm}{d\tau} &= \frac{1}{\tau_m \hat{t}_m(v)}(m_\infty(v) - m) \\
 \frac{1}{\hat{T}_h k_t} \frac{dh}{d\tau} &= \frac{1}{\tau_h \hat{t}_h(v)}(h_\infty(v) - h) \\
 \frac{1}{\hat{T}_n k_t} \frac{dn}{d\tau} &= \frac{1}{\tau_n \hat{t}_n(v)}(n_\infty(v) - n).
 \end{aligned}
 \tag{2.11}$$

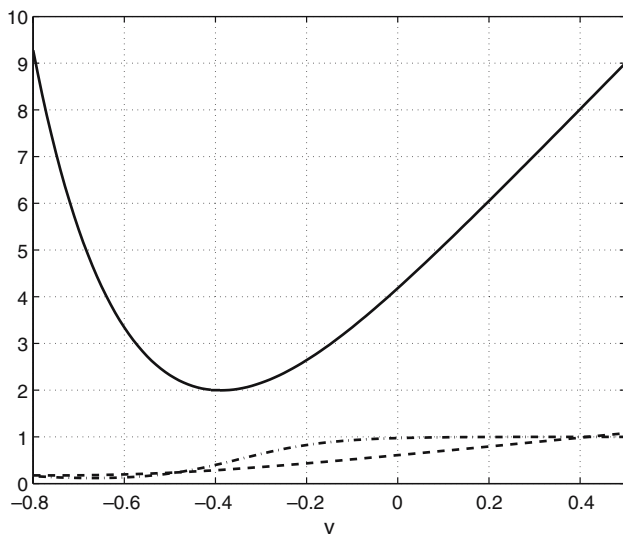


Fig. 3 Functions $1/\hat{\tau}_m(v)$ (solid), $1/\hat{\tau}_h(v)$ (dash-dotted), and $1/\hat{\tau}_n(v)$ (dashed); all in $(\text{ms})^{-1}$

Note that (C/g_{Na}) and $(1/\hat{T}_m)$ are fast reference times (≤ 0.1 ms) while $(1/\hat{T}_h)$ and $(1/\hat{T}_n)$ are slow reference times (≈ 1 ms).

Our aim is to understand the long delays of action potentials, so we choose the given slow time scale $1/\hat{T}_h \approx 1/\hat{T}_n \approx 1$ ms as a reference time and set $k_t = 1$ ms. With that setting, the two dimensionless parameters $C/(k_t g_{Na})$ and $1/(\hat{T}_m k_t)$ on the left hand side are small. Since the activation of the sodium channel m is directly related to the dynamics of the membrane (action) potential v , we assume that (v, m) evolve on the same fast time scale and set

$$\varepsilon := \frac{C}{k_t \cdot g_{Na}} \ll 1, \quad \frac{1}{\hat{T}_m k_t} := \frac{\varepsilon}{T_m} \ll 1. \tag{2.12}$$

Furthermore we define $\hat{T}_h k_t =: T_h$ and $\hat{T}_n k_t =: T_n$ so that each T_x is a dimensionless parameter. With these definitions we obtain finally the HH equations in dimensionless form and as a singularly perturbed system

$$\begin{aligned} \varepsilon \frac{dv}{d\tau} &= [\bar{I} - m^3 h (v - \bar{E}_{Na}) - \bar{g}_k n^4 (v - \bar{E}_K) - \bar{g}_l (v - \bar{E}_L)] \\ \varepsilon \frac{dm}{d\tau} &= \frac{1}{\tau_m t_m(v)} (m_\infty(v) - m) \\ \frac{dh}{d\tau} &= \frac{1}{\tau_h t_h(v)} (h_\infty(v) - h) \\ \frac{dn}{d\tau} &= \frac{1}{\tau_n t_n(v)} (n_\infty(v) - n) \end{aligned} \tag{2.13}$$

with (v, m) as fast variables, (h, n) as slow variables and $t_x(v) := \hat{t}_x(v)/T_x$. This reflects exactly the assumptions made in the pioneering work of FitzHugh (1960). The significantly faster activation of the sodium channel m than its

inactivation h and the activation of the potassium channel n makes the creation of action potentials possible.

Remark 1 A misleading statement about the HH system is often found in the literature, namely that the gate m evolves on the fastest time scale in this system. The correct statement is that m evolves faster than the other two gating variables, which is essential for the creation of action potentials, but m actually evolves slower than the membrane potential V (i.e., the parameter $T_m < 1$). One could argue that the HH system evolves on three different time scales: V fast, m intermediate and (h, n) slow. But to apply classical singular perturbation techniques, which allow for just two different time scales, we group (V, m) as fast and (h, n) as slow, based on (2.12), as described above.

2.2 Reduction to 3D model

By setting $\varepsilon = 0$ in the 4D singularly perturbed system (2.13) we obtain the *reduced system* (also called the slow subsystem). This system is a differential algebraic system describing the evolution of the slow variables (n, h) constrained to a 2D manifold S_0 , called the critical manifold, which is defined by the two equations

$$\begin{aligned} n^4(v, m, h) &= \frac{\bar{I} - m^3 h (v - \bar{E}_{Na}) - \bar{g}_l (v - \bar{E}_L)}{\bar{g}_k (v - \bar{E}_K)}, \\ m(v, n, h) &= m_\infty(v). \end{aligned}$$

If we project S_0 into the (v, n, h) space by using the identity $m = m_\infty(v)$, then S_0 is defined by

$$n^4(v, h) = \frac{\bar{I} - m_\infty(v)^3 h (v - \bar{E}_{Na}) - \bar{g}_l (v - \bar{E}_L)}{\bar{g}_k (v - \bar{E}_K)}. \tag{2.14}$$

This critical manifold S_0 is a cubic shaped surface as shown in Fig. 4, a typical feature of relaxation oscillators in general. The slow dynamics on the critical manifold describes e.g. the slow depolarization towards the action potential threshold shown in Fig. 1. Whenever the neuron fires an action potential, it changes to a fast dynamics where the slow variables are (almost) constant but the fast variables change rapidly. This behaviour is described by the *layer problem* (or fast subsystem)

$$\begin{aligned} \frac{dv}{d\tau_1} &= [\bar{I} - m^3 h_0 (v - \bar{E}_{Na}) - \bar{g}_k n_0^4 (v - \bar{E}_K) - \bar{g}_l (v - \bar{E}_L)] =: f(v, m) \\ \frac{dm}{d\tau_1} &= \frac{1}{\tau_m t_m(v)} (m_\infty(v) - m) =: g(v, m), \end{aligned} \tag{2.15}$$

which is obtained by changing to the fast time $\tau_1 = \tau/\varepsilon$ and taking the limit $\varepsilon \rightarrow 0$. The slow variables $h = h_0$ and $n = n_0$ are now constants. The critical manifold S_0 is the

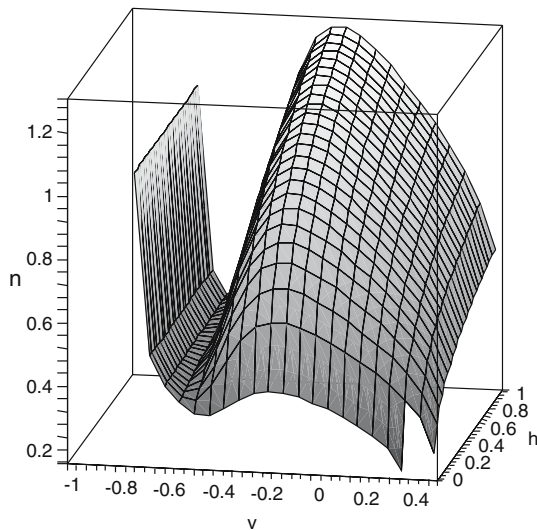


Fig. 4 Cubic shaped critical manifold S_0 of the dimensionless HH system shown in (v, h, n) space, $I_0 = 9.6$

manifold of equilibria for the layer problem, and trajectories of the layer problem evolve along one-dimensional sets (v, h_0, n_0) , called *fast fibers*, near this manifold S_0 . If we linearize the layer problem at S_0 we obtain information about the transient behaviour of solutions along these fast fibers, in the neighborhood of this manifold. It is well known that solutions are quickly attracted along the fast fibers to one of the outer two attracting branches of the critical manifold and, to leading order, follow the reduced flow towards the associated fold curve. In the neighbourhood of the fold curve the dynamics changes significantly and the layer problem will eventually cause a fast transient behaviour towards the other attracting branch observed e.g. as an upstroke in the action potential.

The following result shows that the transient behaviour near the fold is described by a 3D vector field representing the flow on a 3D center manifold of (2.13); for a more general result see (Brøns et al. 2006).

Theorem 1 *The vector field (2.13) on the fast time scale $\tau_1 = \tau/\varepsilon$ possesses a three dimensional center manifold M along the fold curve, which is exponentially attracting. The vector field (2.13) reduced to M is given by:*

$$\begin{aligned} \varepsilon \frac{dv}{d\tau} &= [\bar{I} - m_\infty^3(v)h(v - \bar{E}_{Na}) - \bar{g}_k n^4(v - \bar{E}_K) \\ &\quad - \bar{g}_l(v - \bar{E}_L)] =: F(v, n, h) \\ \frac{dh}{d\tau} &= \frac{1}{\tau_h \cdot t_h(v)}(h_\infty(v) - h) =: H(v, h) \\ \frac{dn}{d\tau} &= \frac{1}{\tau_n \cdot t_n(v)}(n_\infty(v) - n) =: N(v, n). \end{aligned} \tag{2.16}$$

Proof Introducing a new variable $\bar{m} = m - m_\infty(v)$ in system (2.13) on the fast time scale $\tau_1 = \tau/\varepsilon$ gives the layer problem

$$\begin{aligned} \frac{dv}{d\tau_1} &= [\bar{I} - (m_\infty(v) + \bar{m})^3 h(v - \bar{E}_{Na}) \\ &\quad - \bar{g}_k n^4(v - \bar{E}_K) - \bar{g}_l(v - \bar{E}_L)] =: f(v, \bar{m}) \\ \frac{d\bar{m}}{d\tau_1} &= -\frac{1}{\tau_m t_m(v)} \bar{m} - m'_\infty(v) f(v, \bar{m}) =: \bar{g}(v, \bar{m}) \end{aligned} \tag{2.17}$$

The critical manifold S_0 is defined by $\{f(v, \bar{m}) = 0, \bar{m} = 0\}$. Hence

$$\left. \frac{\partial \bar{g}}{\partial v} \right|_{S_0} = -m'_\infty(v) \left. \frac{\partial f}{\partial v} \right|_{S_0}.$$

Furthermore

$$\begin{aligned} \left. \frac{\partial \bar{g}}{\partial \bar{m}} \right|_{S_0} &= -\frac{1}{\tau_m t_m(v)} - m'_\infty(v) \left. \frac{\partial f}{\partial \bar{m}} \right|_{S_0} < 0, \\ \text{since } \left. \frac{\partial f}{\partial \bar{m}} \right|_{S_0} &= -3m_\infty^2(v)h(v - \bar{E}_{Na}) > 0 \end{aligned}$$

and $m'_\infty > 0$. It follows that the Jacobian

$$\left(\begin{array}{cc} \frac{\partial f}{\partial v} & \frac{\partial f}{\partial \bar{m}} \\ \frac{\partial \bar{g}}{\partial v} & \frac{\partial \bar{g}}{\partial \bar{m}} \end{array} \right) \Big|_{S_0}$$

has a single zero eigenvalue whenever $(\partial f/\partial v)|_{S_0} = 0$, which happens along the fold curve. In that case the Jacobian is given by

$$\left(\begin{array}{c} 0 \quad \frac{\partial f}{\partial \bar{m}} \\ 0 \quad \frac{\partial \bar{g}}{\partial \bar{m}} \end{array} \right)$$

Therefore the eigenvector for the zero eigenvalue is given by $(v, \bar{m}) = (1, 0)$ and the center manifold is approximately given by $\bar{m} = 0$. The statement follows. \square

Remark 2 This local center manifold reduction near the fold curve is one of the classical global reduction steps (i.e., setting $m = m_\infty(v)$) in the literature. The global reduction is basically justified by the fact that the dynamics away from the fold curves is slaved to the reduced flow of the two attracting branches of the critical manifold.

The center manifold reduction resembles an instantaneous approach of the gating variable m to its equilibrium state $m = m_\infty(V)$. The activation speed of m is fast compared to that of the other two gating variables (n, h) , but it is actually modest compared to the dynamics of the membrane potential v . So we have to expect quantitative changes in the reduced 3D model (2.16) compared to the full HH model (2.13). Indeed, we observe for the classical case $(\tau_x = 1, x = m, n, h)$, a subcritical Hopf bifurcation occurs at an injected current of $I \approx 9.75$, whereas the onset of firing of action potentials in the full HH model arises for $I \approx 6.25$, where a family of stable periodic orbits is born in a saddle-node bifurcation. In contrast, in the 3D model (2.16), the subcritical Hopf

bifurcation shifts to $I \approx 7.75$, and we observe the onset of oscillations via a saddle-node bifurcation of periodic orbits already for $I \approx 4.06$. This earlier onset reflects the increased speed of activation of the sodium channels.

Remark 3 Note that we are varying the original applied current I , which changes the dimensionless parameter $\hat{I} = I/(k_v \cdot g_{Na})$ in systems (2.13) and (2.16). This is done for easier comparison with results on the original system (1.1).

Remark 4 In the following analysis we consider $\tau_h \geq 1$ and $\tau_n \geq 1$. These assumptions for system (2.16) guarantee the time scale separation between the v and (h, n) dynamics ($1/\varepsilon : 1$) as derived in Subsect. 2.1. Note that in the case $\tau_{\min} := \min\{\tau_h, \tau_n\} < 1$ a rescaling of time $\tau = \tau_{\min} \tilde{\tau}$ leads to a transformed system (2.16) with $\tilde{\varepsilon} = \varepsilon/\tau_{\min}$, $\tilde{\tau}_h = \tau_h/\tau_{\min} \geq 1$ and $\tilde{\tau}_n = \tau_n/\tau_{\min} \geq 1$. If $\tilde{\varepsilon} \ll 1$, then the following singular perturbation analysis still applies.

Remark 5 The standard 2D reduction, which includes the center manifold ($m = m_\infty(v)$), uses the relation $h = 0.8 - n$, but this was obtained for 18.5°C, using a different reduction approach (Rinzel 1985). The best empirical linear fit to the silent phase part of an action potential from the original 4D system is $h = 0.91 - 1.14n$, while the best linear fit to the 3D system (2.16) is $h = 0.9 - 1.05n$. Interestingly, the reduction using $h = 0.8 - n$ restores the onset of action potentials to $I \approx 6.3$. As far as we are aware, this is coincidental.

The 2D critical manifold S_0 of the 3D singularly perturbed system (2.16) is given by (2.14) and shown in Fig. 4. Clearly, the 1D fast vector field is tangent at folds, i.e. the eigenvalue of the 1D layer problem is zero there. The folds represent saddle-node bifurcations of the layer problem. The outer branches of S_0 are attracting while the inner branch is repelling. The reduced 3D HH system (2.16) is a singularly perturbed system in a form suitable for a geometric analysis.

3 Geometric analysis of singularly perturbed systems

The cubic shape of the critical manifold S_0 (2.14) allows system (2.16) to exhibit relaxation oscillation type solutions. There is the possibility of (classical) relaxation oscillations as shown in Fig. 2 (left), or more complicated dynamics like mixed mode oscillations shown in Fig. 2 (right), just to name two possibilities. The main difference in the dynamics between these two cases occurs near the lower fold of the critical manifold, where the flow either jumps immediately to the upper branch and creates an action potential or stays longer near the fold and produces subthreshold oscillations before jumping. In this section, we show how one deduces these oscillatory behaviours from properties of the singular limit systems obtained from (2.16).

3.1 Relaxation oscillations

Relaxation oscillations in 3D systems with 1 fast and 2 slow variables and a structure like the reduced HH system (2.16) were studied by Szmolyan and Wechselberger (2004), Brøns et al. (2006) and Guckenheimer et al. (2005), based on geometric singular perturbation theory (Fenichel 1979; Jones 1995; for an overview see Wechselberger 2005b). The basic assumption in the geometric singular perturbation analysis is that the critical manifold is cubic shaped, as is true for the HH model (2.16). Let $S_0 := \{(v, h, n) \in \mathbb{R}^3 : F(v, h, n) = 0\}$.

Assumption 1 *The manifold $S := \{(v, h, n) \in S_0 : h \in [0, 1]\}$ is ‘cubic-shaped’, i.e. $S = S_a^- \cup L^- \cup S_r \cup L^+ \cup S_a^+$ with attracting upper and lower branches $S_a^\pm, S_a^+ \cup S_a^- := \{(v, h, n) \in S : F_v(v, h, n) < 0\}$, a repelling branch $S_r := \{(v, h, n) \in S : F_v(v, h, n) > 0\}$ and fold curves $L^\pm, L^+ \cup L^- := \{(v, h, n) \in S : F_v(v, h, n) = 0, F_{vv}(v, h, n) \neq 0\}$.*

We would like to describe relaxation oscillations in their singular limit. Note that for sufficiently small values of the perturbation parameter, $0 < \varepsilon \ll 1$, fast jumps are executed near the lower fold curve. In the singular limit, we describe these jumps as projections along the fast fibers of the layer problem onto the other attracting branch of the critical manifold.

After the jump, the trajectory follows the reduced flow until it reaches the other fold curve, where it gets projected back along another fast fiber onto the first attracting branch of the critical manifold. Let $P(L^\pm) \subset S_a^\mp$ be the projection along the fast fibers of the fold curve L^\pm onto the opposite attracting branch S_a^\mp .

Definition 1 A singular periodic orbit Γ of system (2.16) is a piecewise smooth closed curve $\Gamma = \Gamma_a^- \cup \Gamma_f^- \cup \Gamma_a^+ \cup \Gamma_f^+$ consisting of solutions $\Gamma_a^\pm \subset S_a^\pm$ of the reduced system connecting points of the projection curves $P(L^\mp) \subset S_a^\pm$ and the fold curves L^\pm , where these slow solutions are connected by fast fibers Γ_f^\pm from L^\pm to $P(L^\pm)$.

Assumption 2 *There exists a singular periodic orbit Γ for system (2.16).*

We show in Sect. 4 that this assumption is usually fulfilled for sufficiently large injected current I_0 .

A sketch of a singular periodic orbit is shown in Fig. 5. The existence of such a singular periodic orbit can be shown in the following way:

- Show the existence of subsets $N^\pm \subseteq P(L^\mp)$ with the property that all trajectories of the reduced flow with initial conditions in N^\pm reach the fold curve L^\pm (in finite time). It follows that the associated maps $\Pi^\pm : N^\pm \subseteq P(L^\mp) \mapsto L^\pm$ are well defined.

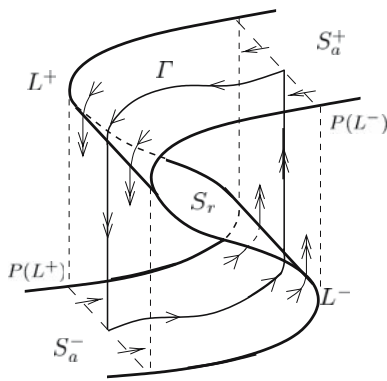


Fig. 5 Schematic illustration of a critical manifold S and singular periodic orbit Γ leading to classical relaxation oscillations. Both fold points of the singular orbit Γ are jump points

- If the return map $\Pi := P \circ \Pi^+ \circ P \circ \Pi^- : N^- \mapsto P(L^+)$ is also well defined and has the property that $\Pi(N^-) \subset N^-$ then, by Brouwer’s fixed point theorem, the existence of a singular periodic orbit follows, i.e. a fixed point of the return map exists. Uniqueness of the fixed point would follow if Π is a contraction.

The key to finding singular periodic orbits Γ is to calculate the reduced flow on the critical manifold S and to find solutions Γ_a^\pm . Recall that, based on (2.14), S is given as a graph $n(h, v)$, $h \in [0, 1]$, $v \in \mathbb{R}$, along which $F(v, n, h) = 0$. Thus, we define a projection of the reduced system onto the (h, v) -plane. Implicitly differentiating $F(v, n, h) = 0$ with respect to time gives the relationship $F_v \dot{v} = -(F_h H + F_n N)$ and we obtain

$$\begin{pmatrix} 1 & 0 \\ 0 & -F_v \end{pmatrix} \begin{pmatrix} \dot{h} \\ \dot{v} \end{pmatrix} = \begin{pmatrix} H \\ F_n N + F_h H \end{pmatrix}. \tag{3.18}$$

The equation for \dot{v} is singular along the fold curves, $F_v = 0$. Therefore we rescale time to obtain the *desingularized reduced flow* on the critical manifold. Using \dot{h}, \dot{v} to represent differentiation with respect to rescaled time, this system takes the form

$$\begin{pmatrix} \dot{h} \\ \dot{v} \end{pmatrix} = \begin{pmatrix} -F_v H \\ F_n N + F_h H \end{pmatrix}. \tag{3.19}$$

This system has the same phase portrait as the reduced system (3.18), but the orientation of trajectories is reversed on S_r , where $F_v > 0$. The local dynamics near the fold curves L^\pm can be completely understood from analysis of (3.19). Typically, fold points $p \in L^\pm$ are jump points and are defined by the normal switching condition

$$(F_n N + F_h H)|_{p \in L^\pm} \neq 0. \tag{3.20}$$

Under this condition the reduced flow (3.18) becomes unbounded along the fold curve L^\pm . Thus trajectories of system (2.16) reaching the vicinity of L^\pm subsequently jump

away from the fold. This jumping behaviour near L^\pm is part of the mechanism leading to (classical) relaxation oscillations in system (2.16) shown in Figure 2 (left). The following assumptions guarantee the existence of such (periodic) relaxation oscillations.

Assumption 3 *The two fold points $p \in L^\pm$ of the singular periodic orbit Γ are jump points, i.e. (3.20) is fulfilled.*

Assumption 4 *The singular periodic orbit is transversal to the curves $P(L^\mp)$ on S_a^\pm .*

Theorem 2 (Szmolyan and Wechselberger 2004) *Given system (2.16) under Assumptions 1–4, there exists generically a periodic relaxation orbit for sufficiently small ε .*

This theorem shows under which conditions trains of classical action potentials can be found (Fig. 2, left). Obviously, if the singular periodic orbit is obtained by the contraction mapping principle as described above then the periodic relaxation orbit is a (local) attractor. If the periodic orbit follows from Brouwer’s fixed point theorem, then we also know that there exists a periodic relaxation orbit that is a local attractor but additional periodic orbits could also exist. For more details on relaxation oscillations we refer to (Szmolyan and Wechselberger 2004).

3.2 Excitable state

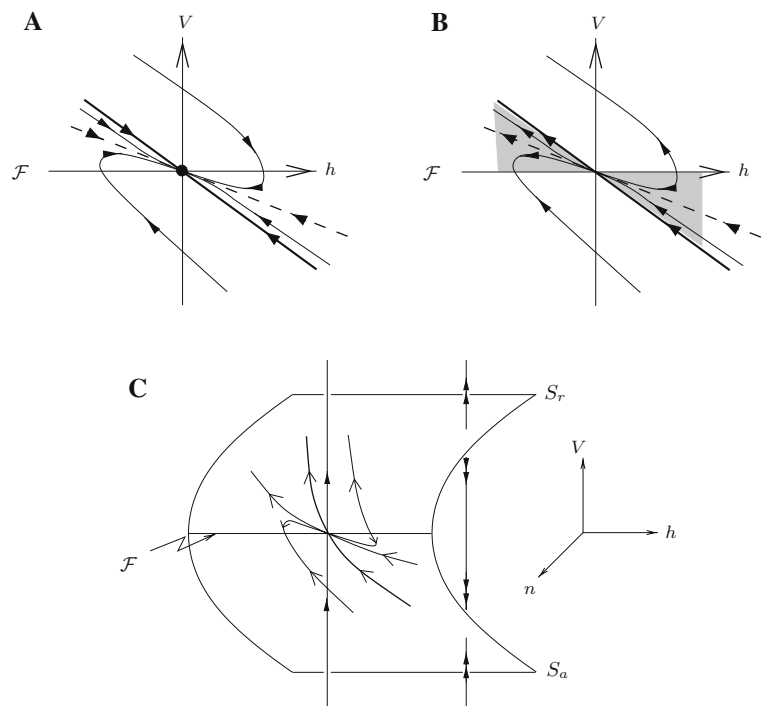
The approach described above for the calculation of a singular periodic relaxation oscillation assumes that there are no equilibrium points of the reduced flow on S_a^\pm between the subsets $N^\pm \subseteq P(L^\mp)$ and the fold curves L^\pm . If there exists an equilibrium of the reduced flow, e.g. on the lower branch S_a^- , then this equilibrium is usually stable and its basin of attraction includes a subset $\tilde{N}^- \subset P(L^+)$. For such initial conditions the map Π is not defined and we expect the system to be in an excitable state.

Proposition 1 *Consider system (2.16) under Assumption 1. If there exists a stable equilibrium on the lower attracting branch S_a^- that is a local (global) attractor of the reduced flow, then there exists a local (global) attractor for sufficiently small ε .*

If the conditions described in Proposition 1 hold, then the system is said to be locally (globally) in an excitable state. The strategy to show excitability is as follows:

- Identify the subset $\tilde{N}^- \subseteq P(L^+)$ that lies in the basin of attraction of the equilibrium on the lower attracting branch. If $\tilde{N}^- = P(L^+)$, then the equilibrium is a global attractor.
- Otherwise, take the complementary subset $(\tilde{N}^-)^c \subset P(L^+)$ and check whether $\Pi((\tilde{N}^-)^c) \subset \tilde{N}^-$, i.e. whether

Fig. 6 Schematic illustration of the reduced flow near a folded node singularity. **a** The desingularized flow near a node singularity. The *bold curve* corresponds to the strong stable eigendirection of the node while the *dashed curve* corresponds to the weak eigendirection of the node. The fold \mathcal{F} lies on the z -axis. **b** The reduced flow near the folded node singularity obtained from A by reversing the flow on S_r ($x > 0$). All trajectories on S_a^- ($x < 0$) within the shadowed region are funnelled through the folded node singularity to S_r ($x > 0$). These trajectories are called singular canards. The *bold trajectory* is called the primary strong canard while the *dashed trajectory* is called the primary weak canard. **c** 3D representation of the reduced flow on the critical manifold



the return map Π maps the complementary subset into the basin of attraction of the equilibrium. If this condition holds, then the equilibrium is a global attractor. If not, then the equilibrium is just a local attractor and may co-exist with (an)other local attractor(s), e.g. singular periodic relaxation oscillations. Which local attractor a trajectory will approach then depends on the corresponding initial condition of system (2.16).

3.3 MMO's and canards

MMO's consist of L large amplitude (relaxation) oscillations followed by s small amplitude (sub-threshold) oscillations, and the symbol L^s is assigned to this pattern. The subthreshold oscillations of such MMO patterns can be explained by *folded singularities* of the reduced flow as described in (Milik et al. 1998; Wechselberger 2005a; Brøns et al. 2006). Typically, a folded singularity is an isolated point $p \in L^\pm$ which violates the normal switching condition (3.20). Since $F_v = 0$ on L^\pm , a folded singularity is an equilibrium of the desingularized flow (3.19).

Definition 2 We call $p \in L^\pm$ a folded node, folded saddle, or folded saddle-node if, as an equilibrium of (3.19), it is a node, a saddle, or a saddle-node.

For MMO's to exist, folded nodes (or, in the limiting case, folded saddle-nodes) are required. A typical phase portrait of the reduced flow near a folded node is shown in Fig. 6. Note that there exists a whole sector of solutions (shadowed region) that is funnelled through the folded node singularity

to the repelling branch S_r of the critical manifold. Solutions with such a property are called *singular canards* and are a direct consequence of the existence of a folded singularity.

The sector of singular canards is called the *funnel* of the folded node singularity. For a detailed introduction to canard solutions we refer to (Szmolyan and Wechselberger 2001; Wechselberger 2005a; Brøns et al. 2006) and references therein. The borders of the funnel are given by the fold curve (\mathcal{F} in Fig. 6) and the so called *primary strong canard*. This primary strong canard is the solution of the reduced flow (3.19) that corresponds to the unique strong eigendirection of the folded node singularity. All other singular canards are tangent to the so called *primary weak canard* corresponding to the weak eigendirection of the folded node.

The following assumption is needed for the existence of MMO's as shown e.g. in Fig. 2, right:

Assumption 5 The fold point $p^- \in L^-$, where the singular periodic orbit Γ intersects L^- , is a folded node (folded saddle-node) singularity, while the fold point $p^+ \in L^+$, where Γ intersects L^+ , is a jump point.

Theorem 3 (Brøns et al. 2006) Suppose that system (2.16) satisfies Assumptions 1–2,4–5. If the segment Γ_a^- of the singular periodic orbit Γ is in the interior of the singular funnel, then for sufficiently small ε , there exists a stable periodic orbit of MMO type 1^s for some $s > 0$.

Actually, it is possible to calculate the (maximal) number of small oscillations s of this 1^s MMO pattern. Define $\mu := \lambda_1/\lambda_2 < 1$ as the ratio of the eigenvalues $\lambda_{1/2}$ ($|\lambda_1| \leq$

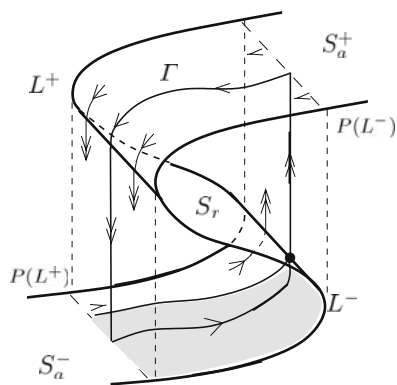


Fig. 7 Critical manifold S and singular periodic orbit Γ leading to MMO's. The fold point in the silent phase of the singular orbit Γ is a canard point (folded node/folded saddle-node singularity), while the fold point in the active phase is a jump point

$|\lambda_2|)$ corresponding to the node singularity of the desingularized flow (3.19). Then the number of maximal subthreshold oscillations is given by (Wechselberger 2005a)

$$s = s(\mu) = \left\lfloor \frac{1 + \mu}{2\mu} \right\rfloor \tag{3.21}$$

where the right hand side denotes the greatest integer less than or equal to $(1 + \mu)/(2\mu)$. Different MMO patterns $L^{s'}$ with $L \geq 1$ and $s' < s$ can just be obtained under the variation of an additional parameter in system (2.16) that changes the global return mechanism.

Theorem 4 (Brøns et al. 2006) *Suppose that system (2.16) satisfies Assumptions 1–2,4–5. Assume that there exist a parameter β in system (2.16) and a value β_0 such that for $\beta = \beta_0$, the segment Γ_a^- of the singular periodic orbit Γ consists of a segment of the primary strong canard. Then the following holds, provided ε is sufficiently small: For each $1 \leq s' < s$, there exists an interval $J_{s'}$ with length of order $O(\varepsilon^{\frac{1-\mu}{2}})$ such that if $\beta \in J_{s'}$, then a stable $1^{s'}$ MMO pattern exists.*

A sketch of a singular periodic orbit Γ leading to MMO's is given in Fig. 7. The existence of such a singular periodic orbit can be shown as follows:

- Calculate the return map Π for a single initial condition in $P(L^+)$ that lies within the basin of attraction of the folded node resp. folded saddle-node singularity (the funnel) and show that this initial condition is mapped back into the funnel by Π . This guarantees immediately the existence of a unique singular periodic orbit fulfilling Assumption 5, since all trajectories within the singular funnel are contracted to the folded singularity.

The small (subthreshold) oscillations observed in a MMO pattern occur in the neighbourhood of the folded node

singularity. The reason can be roughly explained as follows: Note that existence and uniqueness of solutions of system (2.16) for small $\varepsilon \neq 0$ is guaranteed. In the singular limit, however, uniqueness is lost for the reduced flow along the fold curve. In particular, at the folded node singularity we have a continuum of solutions, the singular canards, passing from the attracting branch S_a through one single point, the folded node singularity, to the repelling branch S_r as described above. Wechselberger (2005a) showed that a discrete number of canard solutions persist under small perturbations $0 < \varepsilon \ll 1$, i.e. all these canard solutions connect from the attracting branch $S_{a,\varepsilon}$ to the repelling branch $S_{r,\varepsilon}$. The existence of invariant manifolds $S_{a,\varepsilon}$ and $S_{r,\varepsilon}$ away from the fold, which are $O(\varepsilon)$ perturbations of S_a and S_r , are guaranteed by Fenichel theory (Fenichel 1979; Jones 1995). Furthermore, solutions of (2.16) on $S_{a,\varepsilon}$ and $S_{r,\varepsilon}$ will approximately follow the reduced flow on S_a and S_r . By a pure topological argument it follows that the only way for canard solutions to connect these manifolds $S_{a,\varepsilon}$ and $S_{r,\varepsilon}$ without violating the uniqueness of other solutions nearby is given by rotations of the manifolds $S_{a,\varepsilon}$ and $S_{r,\varepsilon}$ near the fold curve. For a more detailed explanation of this geometric structure we refer to (Guckenheimer and Haiduc 2005; Wechselberger 2005a).

Theorem 4 states that under the variation of an additional parameter β in system (2.16), which changes the global return mechanism, MMO patterns of type $1^{s'}$ with $1 \leq s' < s$ are realized. Combinations of adjacent MMO patterns $1^{s'}$ and $1^{s'+1}$ are usually observed in the transition from one stable MMO pattern $1^{s'+1}$ to another stable MMO pattern $1^{s'}$ under variation of β . Within the transition from a 1^1 MMO pattern to relaxation oscillations (1^0 MMO pattern) one may also observe L^1 patterns, $L > 1$, as well as combinations of patterns. More complex $L^{s'}$ MMO patterns as well as related combinations are found for $\mu \rightarrow 0$, such that $s(\mu) \rightarrow \infty$, and/or for larger ε . These complex patterns are not well covered by the current theory and the development of such a theory will be the focus of future work.

4 Analysis of the 3D HH system (2.16)

In the following we show under which conditions on the parameters of system (2.16) we obtain either an excitable system, relaxation oscillations or MMO's.

4.1 Singularities of the reduced flow

To analyse the reduced flow (3.18) on the critical manifold S , we calculate the desingularized system (3.19) as described in Sect. 3 for the 3D HH system (2.16) and check under

which conditions we find singularities. The right hand side functions of (3.19) are given by

$$\begin{aligned}
 F_v &= -(m_\infty^3(v) h + \bar{g}_k n^4(v, h) + \bar{g}_l + 3m_\infty^2(v) h (v - \bar{E}_{Na}) m'_\infty(v)) \\
 F_h &= -(m_\infty(v) (v - \bar{E}_{Na})) \\
 F_n &= -(4\bar{g}_k n^3(v, h) (v - \bar{E}_K))
 \end{aligned}$$

and $n(v, h)$ is defined in (2.14). Recall that the folds L^\pm are defined by $F_v = 0$. The functions H and N depend on the time constants τ_h and τ_n . Each of the functions F_v , F_h and F_n depends on the parameter I .

There are two classes of equilibria of system (3.19). The first occurs where $H = 0$, corresponding to $h = h_\infty(v)$, and $N = 0$, corresponding to $n(v, h) = n_\infty(v)$, where the function $n(v, h)$ depends on I but not on τ_h and τ_n . Putting this together yields the condition $n(v, h_\infty(v)) = n_\infty(v)$, which has a solution v that is independent of τ_h and τ_n but depends on I , called $v(I)$ below. The second class of equilibria, folded singularities, arises where $F_v = 0$ (along the fold line) and $F_n N + F_h H = 0$. These points depend on τ_h , τ_n and I . There are no equilibria with $H = 0$ and $N \neq 0$, because $F_n \neq 0$.

Remark 6 Both folded and regular singularities are equilibrium points of system (3.19), but only the latter are actually equilibrium points of (3.18), as pointed out in Sect. 3.

A bifurcation occurs as I varies, for fixed τ_h , τ_n , when the the curve of equilibria $v(I)$ intersects the fold $F_v = 0$. This occurs at the special value of I at which

$$F_v(v(I), n(v(I), h_\infty(v(I))), h_\infty(v(I))) = 0.$$

But since the functions $v(I)$, $h_\infty(v)$, $n(v, h)$ are independent of τ_h and τ_n , the location of this bifurcation is independent of τ_h and τ_n as well. Parameter continuation by using XPPAUT (Ermentrout 2002) shows that this bifurcation value is given by $I_c \approx 4.8$. Figures 8, 9 show this bifurcation for different values of τ_h and τ_n , with I taken as the bifurcation parameter. Clearly, the bifurcation point is independent of τ_h and τ_n as claimed, and the bifurcation happens on the fold curve. We will discuss further details about these diagrams below.

Proposition 2 *Generically, the reduced system (3.18) possesses, for $I = I_c \approx 4.8$, a folded saddle-node on the fold curve L^- (independent of τ_h and τ_n). For nearby values $I < I_c$, system (3.18) possesses a folded saddle and a stable node singularity. For nearby values $I > I_c$, system (3.18) possesses a folded node and a saddle singularity. Therefore, the bifurcation of the ordinary and the folded singularity near $I = I_c$ resembles a transcritical bifurcation.*

Remark 7 There exist two different types of folded saddle-node (FSN) singularities. The FSN type I corresponds to a true saddle-node bifurcation of folded singularities, while a FSN type II corresponds to a transcritical bifurcation of a folded singularity with an ordinary singularity

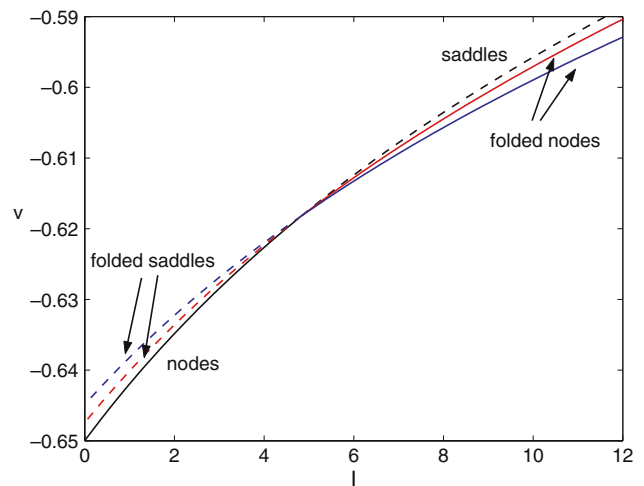


Fig. 8 Bifurcation of equilibria (black regular, other colors folded) for the reduced flow for different values of τ_h ($\tau_h = 1$ (red), $\tau_h = 15$ (dark blue)). Solid curves are asymptotically stable (nodes, folded nodes), while dashed are unstable (saddles, folded saddles). Further details are given in the text

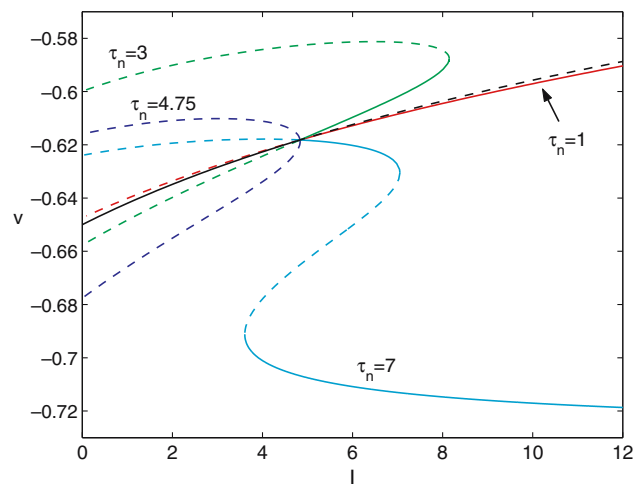


Fig. 9 Bifurcation of equilibria (black: regular, all other colors: folded) for the reduced flow for different values of τ_n . Solid curves are asymptotically stable (nodes), while dashed are unstable (saddles). Further details are given in the text

(Szmolyan and Wechselberger 2001). Therefore, the folded singularity at $I = I_c$ described in Proposition 2 is a FSN type II.

In general, the proposition states that there exists a folded node singularity for certain parameter values. In these cases MMO's are possible, depending on the global return mechanism, as described in Sect. 3. In the following we will split the analysis into 3 different cases: the classical case ($\tau_h = 1, \tau_n = 1$), the case ($\tau_h > 1, \tau_n = 1$) and the case ($\tau_h = 1, \tau_n > 1$).

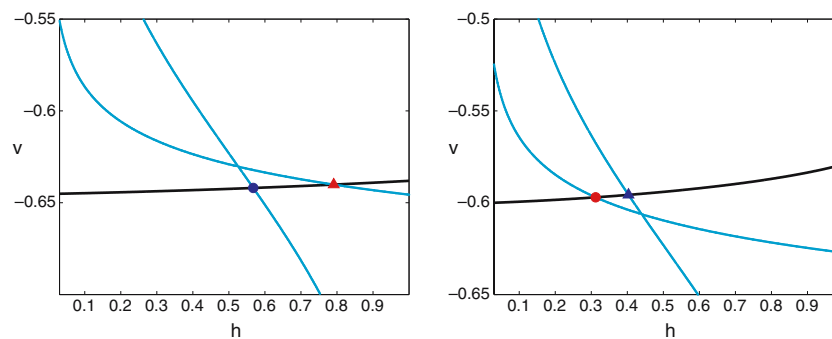


Fig. 10 Phase plane for system (3.19) for the classical case ($\tau_h = 1$, $\tau_n = 1$) with $I = 1 < I_c$ (left) and $I = 10 > I_c$ (right). Note that the cyan curves are the h nullclines and the black curve is the v nullcline for system (3.19). The h nullclines consist of the fold curve $\{F_v = 0\}$,

which intersects the v nullcline in a folded saddle (red triangle) in the left plot, and the curve $\{H = 0\}$, which intersects the v nullcline in a stable node (blue circle) in the left plot

Classical case ($\tau_h = 1$, $\tau_n = 1$)

In that case, system (3.18) has a folded saddle for $0 < I < I_c$, a folded saddle-node type II for $I = I_c$, and a folded node for $I > I_c$ on the lower attracting branch (in the silent phase). Furthermore, the lower attracting branch S_a^- has a stable node for $0 < I < I_c$, which bifurcates via the folded saddle-node singularity to the repelling middle branch S_r , where it becomes a saddle for $I > I_c$ (see Proposition 2).

Figure 10 illustrates these singularities using the nullclines of the desingularized system (3.19) with $I = 1 < I_c$ and $I = 10 > I_c$, respectively. In these as well as analogous phase plane pictures below, the cyan curves are the solutions of $F_v H = 0$, one corresponding to $F_v = 0$ (i.e., the lower fold L^-) and the other corresponding to $H = 0$, while the black curve consists of solutions of $F_n N + F_h H = 0$. Folded equilibria are indicated by red symbols, while regular equilibria are indicated by blue symbols. Finally, nodes are marked with circles, while saddles are marked with triangles. So, in Fig. 10 with $I = 1$ (left), we see a stable node and a folded saddle, while in Fig. 10 with $I = 10$ (right), we see a folded node and a saddle.

Remark 8 There exist two other folded singularities of the reduced flow which have no influence on the dynamics of the classical case, but will become more important in the other two cases ($\tau_h > 1$, $\tau_n = 1$) and ($\tau_h = 1$, $\tau_n > 1$). First, there is another folded saddle in the silent phase for $h \ll 1$. This folded saddle will move to the right for $\tau_n > 1$ (see corresponding case study ($\tau_h = 1$, $\tau_n > 1$) below). Second, there is also a folded focus in the active phase for $h > 1$. This folded focus will move into the physiologically significant range $0 < h < 1$ for $\tau_h > 1$ (see corresponding case study ($\tau_h > 1$, $\tau_n = 1$) below).

Case ($\tau_h > 1$, $\tau_n = 1$)

This case is similar to the classical case. Again, system (3.18) has a folded saddle for $0 < I < I_c$, a folded saddle-node type II for $I = I_c$, and a folded node for $I > I_c$ on the lower attracting branch (in the silent phase), for each fixed $\tau_h > 1$. As in the classical case, the lower attracting branch S_a^- has a stable node for $0 < I < I_c$, which bifurcates via the folded saddle-node singularity to the repelling middle branch S_r , where it becomes a saddle for $I > I_c$ (see Proposition 2). In addition to showing the curve of regular equilibria generated by varying I , Fig. 8 shows examples of how the folded singularities depend on I for $\tau_h = 1$ and $\tau_h = 15$, the former of which is closer to the curve of regular equilibria, illustrating that their dependence on τ_h is quite weak.

The only difference between $\tau_h = 1$ and $\tau_h > 1$ with respect to singularities is that there exists a folded singularity of focus type in the active phase for $\tau_h > \tau_h^f$ within the physiological significant domain $0 < h < 1$. Figure 11 shows the h value of the folded focus for different values of τ_h . At $\tau_h^f \approx 1.4$, the h value is approximately one, while it is less than 1 for $\tau_h > \tau_h^f$. Folded foci do not support canard solutions. The main influence of folded foci on the reduced flow is that they direct the flow a certain way. We shall see in the next two subsections that the folded focus has no significant impact on the solutions that we are studying.

Case ($\tau_h = 1$, $\tau_n > 1$)

As can be seen in Fig. 9, the bifurcation diagram for system (3.19), with bifurcation parameter I , depends much more strongly on τ_n than on τ_h . The black curve in Fig. 9, which switches from solid (for $I < I_c \approx 4.8$) to dashed (for $I > I_c$), is the curve of regular equilibria, which is independent of τ_n , as noted earlier. As τ_n increases from 1, the curve of

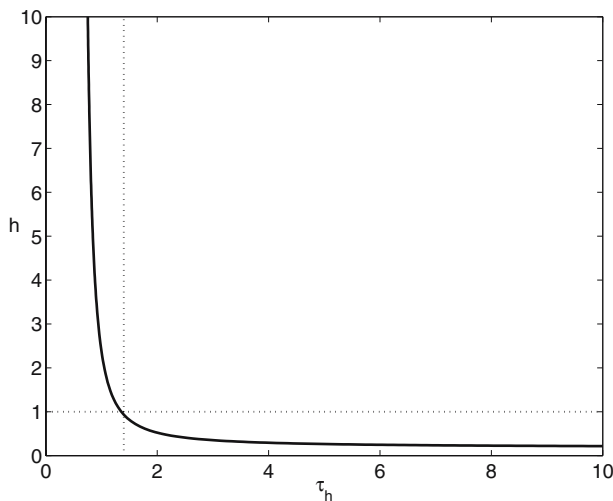


Fig. 11 The h coordinate for the folded focus of system (3.19) depends on τ_h (solid curve). The dotted lines demarcate $h = 1$ and $\tau_h = 1.4$ and illustrate that the focus becomes non-physiological for $\tau_h < \tau_h^f \approx 1.4$

folded equilibria develops two folds, which correspond to saddle-node bifurcations of folded equilibria in the parameter I for each fixed τ_n . Figure 9 shows examples of the curves of folded equilibria for $I > 0$ for a variety of values of τ_n , including $\tau_n = 1$ (red), which is shown for comparison.

We define several critical values of τ_n . First, there exists a value $\tau_n^c \approx 4.75$ such that for all $\tau_n < \tau_n^c$, there is a saddle-node bifurcation of folded equilibria at some $I = I_{SN}^+ > I_c$, lying above the curve of regular equilibria (e.g. $\tau_n = 3$ in Fig. 9). Examples of the corresponding phase planes of (3.19) are shown in Fig. 12 for $I = 1 < I_c$, $I_{SN}^+ > I = 7 > I_c$ and $I = 10 > I_{SN}^+$, which illustrate the following: There exist three singularities in the domain of interest, two folded saddles and one (ordinary) node, for $I = 1$. The folded saddle to the right of the node bifurcates via a transcritical bifurcation at $I = I_c$ to a folded node to the left of the saddle. For $I = I_{SN}^+$ the folded node and the other folded saddle (to the left) annihilate each other in a saddle-node bifurcation and we are only left with a saddle singularity on the repelling side of the critical manifold. Note that the folded saddle-node singularity at $I = I_c$ is of type II, while the folded saddle-node singularity at $I = I_{SN}^+$ is of type I.

For $\tau_n^c < \tau_n < \tau_n^*$ ($\tau_n^* \approx 10.5$), the saddle-node bifurcation at $I_{SN}^+ > I_c$ lies below the curve of regular equilibria, as shown for $\tau_n = 7$ in Fig. 9. Figure 13 shows phase planes for $\tau_n^* > \tau_n = 7 > \tau_n^c$ for $I = 1 < I_c$, for $I = 6$ and $I = 7$, both above I_c and below I_{SN}^+ , and for $I = 10 > I_{SN}^+$. In this case, the folded saddle to the left of the node bifurcates via a transcritical bifurcation at $I = I_c$ to a folded node to the right of the saddle. As I increases towards I_{SN}^+ , a folded saddle from the right ($h > 1$) approaches the folded node. They finally annihilate each other for $I = I_{SN}^+$ in a saddle-node bifurcation. Again, we are left with only a saddle singularity on the repelling side of the critical manifold for $I > I_{SN}^+$.

In both cases, $\tau_n < \tau_n^c$ and $\tau_n^* > \tau_n > \tau_n^c$, a folded node emerges for $I > I_c$ via a transcritical bifurcation and persists up to the saddle-node bifurcation at $I = I_{SN}^+$. In the limit $\tau_n = \tau_n^c$ these two bifurcations merge to a single pitchfork bifurcation at $I = I_c$. This yields a curve of folded saddle equilibria, shown as the $\tau_n = 4.75$ curve in Fig. 9. The value $\tau_n = \tau_n^c$ is the unique value for which the bifurcation at $I = I_c$ is not transcritical and does not create a curve of folded nodes.

As can be seen in Fig. 9 for $\tau_n = 7$, there is also a lower (with respect to I) saddle-node bifurcation of folded equilibria, with a folded node at relatively negative v values for I above this bifurcation. Let I_{SN}^- denote the I value where this lower saddle-node bifurcation occurs. In fact, the interval of τ_n values over which this lower saddle-node exists is given by $(\tau_n^\infty, \tau_n^*)$, where $\tau_n^\infty \approx 4.2$. However, the saddle-node exists for $I_{SN}^- < 0$ for $\tau_n^\infty < \tau_n < \tau_n^- \approx 5.75$, which explains why this bifurcation is not visible in Fig. 9 for $\tau_n^c = 4.75$.

Figure 14 shows both the upper (at $I = I_{SN}^+$, solid) and lower (at $I = I_{SN}^-$, dashed) curves of saddle-node bifurcation points, as functions of τ_n . Note that the two bifurcations come together in a cusp at τ_n^* , which is approximately given by $\tau_n^* \approx 10.5$. Further, as τ_n decreases, the lower saddle-node occurs at progressively larger h and hence becomes physiologically irrelevant. In general, the lower folded nodes have no influence on the dynamics within the physiological relevant boundaries. Therefore, we will not consider them in the following analysis of relaxation oscillations. Note also that the upper saddle-node occurs at progressively larger values $I = I_{SN}^+$ as τ_n decreases towards $\tau_n = 1$, which is why it is not observed in the $\tau_n = 1$ bifurcation curves in Figs. 8, 9. Finally, if $\tau_n > \tau_n^*$, above the cusp of saddle-node bifurcations, then the bifurcation diagram with respect to I becomes more like the classical case again, with a single transcritical bifurcation at $I = I_c$ (within the physiological relevant domain).

To summarize: In all three cases there exists a node singularity for $I < I_c$ on the lower attracting branch (silent phase). In the cases ($\tau_h \geq 1$, $\tau_n = 1$) there exists on L^- a (physiologically relevant) folded node singularity for $I > I_c$. In the case ($\tau_h = 1$, $\tau_n > 1$) there exists on L^- a (physiologically relevant) folded node singularity for $I_{SN}^+ > I > I_c$, where I_{SN}^+ approaches I_c in the (degenerate) limit $\tau_n \rightarrow \tau_n^c$, but $I_{SN}^+ > I_c$ for $\tau_n \neq \tau_n^c$.

4.2 Transversality of reduced flow at $P(L^\pm)$

To apply Theorems 2–4 (relaxation oscillations or MMO’s) we have to show that the associated singular periodic orbit is transversal to the projections of the fold curves $P(L^\pm)$ (Assumption 4). Instead of verifying Assumption 4 for each specific example, we give evidence that the reduced flow is transversal to $P(L^\pm)$ and directed towards the fold curves

Fig. 12 Phase planes for system (3.19) for $\tau_h = 1, \tau_n = 3$: $I = 1 < I_c$ (upper left), $I_{SN}^+ > I = 7 > I_c$ (upper right) and $I = 10 > I_{SN}^+$ (lower)

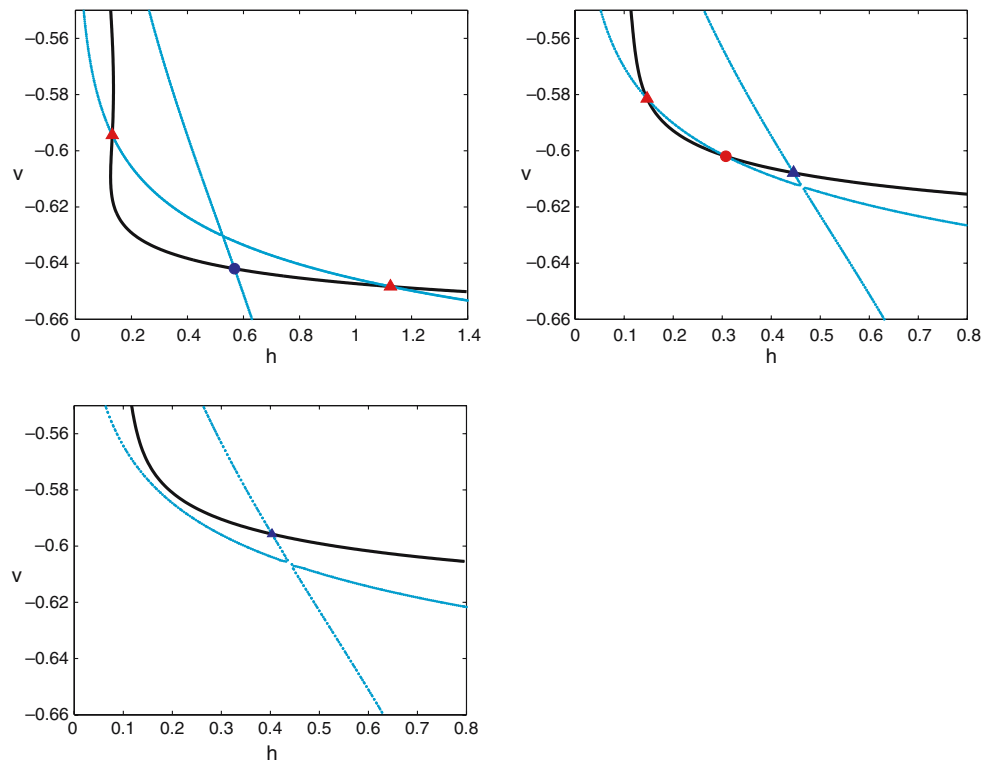
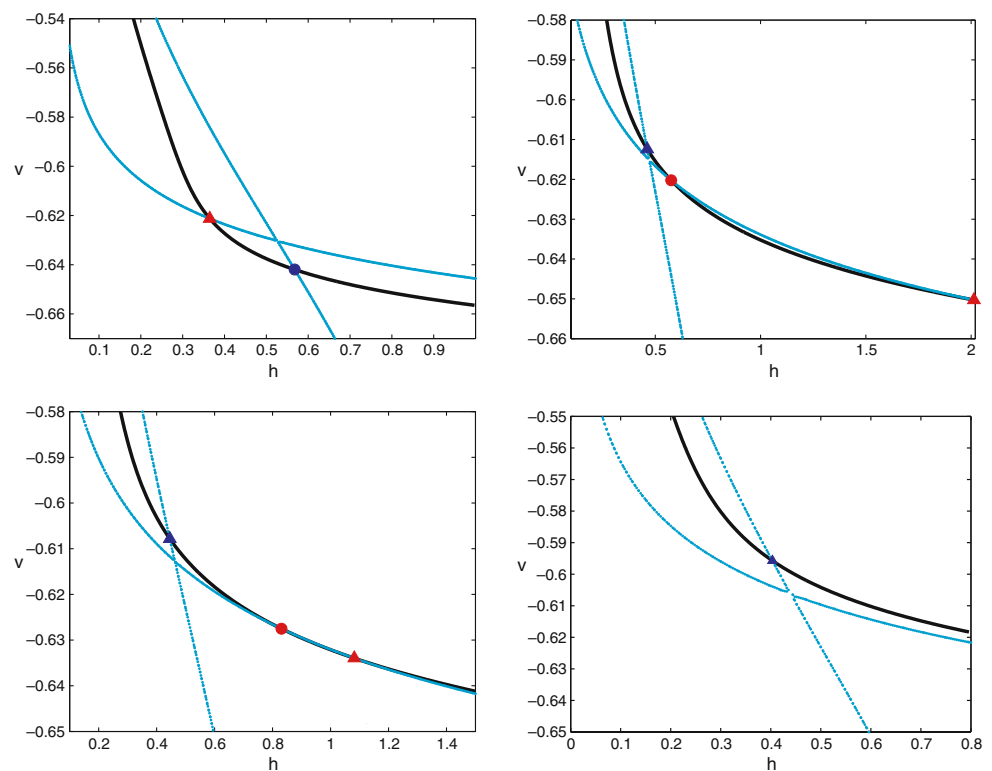


Fig. 13 Phase planes for system (3.19) for $\tau_h = 1, \tau_n = 7$: $I = 1 < I_c$ (upper left), $I_{SN}^+ > I = 6 > I_c$ (upper right), $I_{SN}^+ > I = 7 > I_c$ (lower left) and $I = 10 > I_{SN}^+$ (lower right)



in the whole domain of interest. This more general transversality argument gives important insight into the nature of the reduced flow, since it shows that the reduced flow (Π^-, Π^+) and associated projections preserve the orientation of trajectories. This orientation preservation property will help us to

calculate the return map Π defined in Section 3 in order to find singular periodic orbits.

Proposition 3 *The flow of the reduced system (3.18) is transversal to $P(L^\pm)$ and directed towards L^\mp within the physi-*

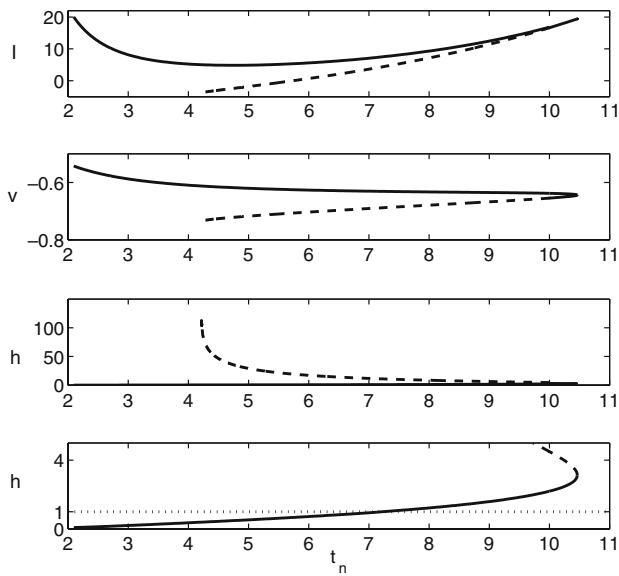


Fig. 14 Curves of saddle-node bifurcations of folded singularities, as functions of τ_n . In each plot, the upper saddle-node (at $I = I_{SN}^+$) is solid and the lower (at $I = I_{SN}^-$) is dashed. Note that the two form a cusp at $\tau_n = \tau_n^* \approx 10.5$, that the I values of the lower curve become negative for $\tau_n < \tau_n^- \approx 5.75$, and that the h values of the lower curve blow up toward a vertical asymptote at $\tau_n = \tau_n^\infty \approx 4.2$ as τ_n decreases. The bottom plot represents a zoomed view, near the cusp, of the plot above it, with a dotted line shown at $h = 1$

ologically relevant domain of h ($0 < h < 1$ but not $h \ll 1$) and the parameter range under study ($I \geq 0, \tau_h \geq 1, \tau_n \geq 1$). Moreover, in this parameter range, the return map Π , where it is defined, preserves the orientation of trajectories, in the sense that if $p_1 = (h_1, v_1), p_2 = (h_2, v_2) \in P(L^+)$ with $h_1 < h_2$, and $\Pi(p_1) = (\hat{h}_1, \hat{v}_1), \Pi(p_2) = (\hat{h}_2, \hat{v}_2)$, then $\hat{h}_1 < \hat{h}_2$.

As with the propositions in Sect. 4.3 below, we use numerical observations to support this proposition. In the discussion below, we omit very small values of h ($h \ll 1$) and consider the rest of the physiological range of h ($0 < h < 1$). All of the statements we make hold independent of the values of I, τ_h, τ_n , within the ranges $I \geq 0, \tau_h \geq 1, \tau_n \geq 1$. We will come back to $h \ll 1$ at the end of the section.

First, note that, as can be seen in Fig. 4 for example, the fold curves L^\pm are almost parallel to the h -axis, as long as h is not too small. Hence, the projections of the fold curves $P(L^\pm)$ are almost parallel to the h -axis, away from very small h , as well. Furthermore, the subsets of the projections $P(L^+)$ and $P(L^-)$ away from $h \ll 1$ lie on opposite sides of the v -nullcline $F_n N + F_h H = 0$ of the reduced flow (3.18). Therefore, \dot{v} has opposite signs along $P(L^+)$ and $P(L^-)$. We can thus use the expressions given in (2.16) to compute numerically, from the desingularized reduced flow (3.19), that in fact $\dot{v} > 0$ along $P(L^+)$ and $\dot{v} < 0$ along $P(L^-)$, away from $h \ll 1$. Since $P(L^\pm)$ are almost parallel to the h -axis, this implies that the reduced flow (3.18) is transver-

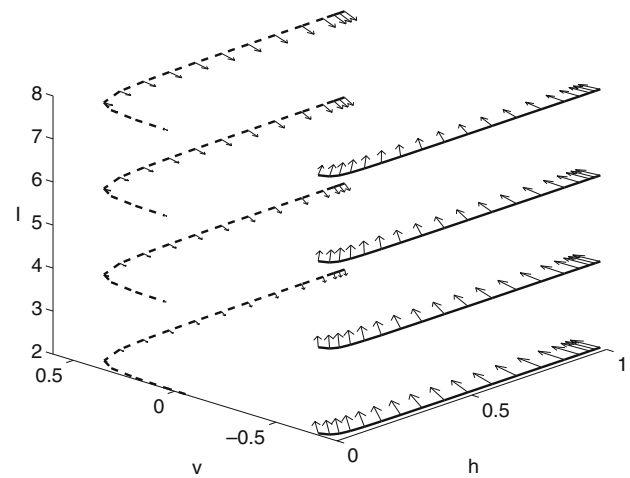


Fig. 15 Transversality of reduced flow at $P(L^+)$ (solid) and $P(L^-)$ (dashed) for $\tau_h = \tau_n = 1$ under variation of I . The arrows indicate the vector field of the reduced system (3.18) at $P(L^\pm)$ and show that the flow is directed towards the fold curves L^\mp (which are not shown here)

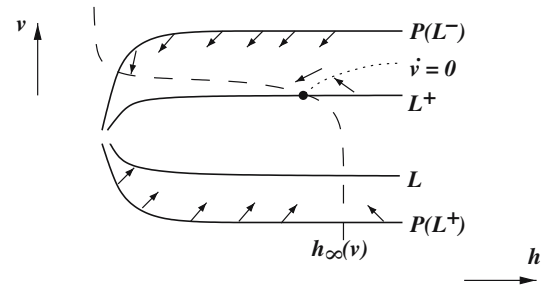


Fig. 16 Illustration of the flow box argument establishing transversality for $0 < h < h_\infty(v)$ on $P(L^+)$, and its inapplicability on $P(L^-)$. The short segments with arrows represent the direction field. The solid circle is the folded focus present in the active phase for $\tau_h > \tau_h^f \approx 1.4$. Note that since the relevant part of $P(L^-)$ lies above $h_\infty(v), \dot{h} < 0$ and transversality cannot be guaranteed there

sal along $P(L^\pm)$ and that the flow is directed towards L^\mp . Figure 15 shows the projection of the fold curves $P(L^\pm)$ together with the reduced vector field from system (3.19) for $\tau_h = \tau_n = 1$ and for different values of I ranging from 2 to 8. These observations reflect the physiological fact that the membrane potential repolarizes in the active phase ($\dot{v} < 0$) and depolarizes in the silent phase ($\dot{v} > 0$). Similar figures can be obtained under variation of τ_h and τ_n and they all support Proposition 3.

For the reduced flow near $P(L^+)$ we can give an even stronger transversality argument for $0 < h < h_\infty(v)$ but not too small, as follows (see Fig. 16): $P(L^+)$ is a convex and monotonically decreasing function with respect to h . If the reduced flow near $P(L^+)$ points into the first quadrant, i.e. $\dot{h} > 0$ and $\dot{v} > 0$, then transversality follows immediately. But we have already given the argument that $\dot{v} > 0$ for $0 < h < 1$ but not too small, while $\dot{h} > 0$ for $0 < h < h_\infty(v)$, and hence transversality follows.

Remark 9 The same argument cannot be used for the reduced flow near $P(L^-)$. Note that $P(L^-)$ is a concave and monotonically increasing function with respect to h . If the reduced flow near $P(L^-)$ pointed into the fourth quadrant, i.e. $\dot{h} > 0$ and $\dot{v} < 0$, then transversality would follow. Again, $\dot{h} > 0$ for $0 < h < h_\infty(v)$, but $h_\infty(v) \ll 1$ for positive v . Therefore, we instead have $\dot{h} < 0$ almost everywhere along $P(L^-)$.

Note that the projections of the fold curves $P(L^\pm)$ become almost parallel to the v -axis, instead of the h -axis, for very small h values, as shown in Figure 15. We take the domain $h \ll 1$ that is excluded from Proposition 3 to consist of the h values where this parallelism occurs. In fact, we found examples where transversality along $P(L^-)$ is violated for $h \ll 1$. Fortunately, it will turn out that such h values are not relevant for our calculations of the return map Π , used to find singular periodic orbits in Sect. 4.3, and hence this exclusion does not affect our ability to analyze the solutions of systems (3.18), (3.19).

Finally, it remains to consider the preservation of orientation under Π . Obviously, the projection P does not change the orientation of trajectories. Moreover, as noted above, the fold curves and their projections are almost parallel to the h -axis for h not too small, while the reduced flow (3.19) is rectifiable between $P(L^+)$ and L^- on S_a^- . Theoretically, orientation of the flow could be affected by the folded focus on $L^+ \subset S_a^+$ for $\tau_h > \tau_h^f$. The focus lies within the intersection $\{(h, v) : F_v = 0\} \cap \{(h, v) : \dot{v} = F_n N + F_h H = 0\}$, and we have already seen that $\dot{v} < 0$ on $P(L^-) \subset S_a^+$, however. Hence, the flow in the neighborhood of the folded focus is counterclockwise in the (h, v) plane (Fig. 16) and trajectories generated by all initial conditions on $P(L^-)$ will intersect L^+ without a change in orientation.

4.3 Singular periodic orbits

In this section, we consider various objects and their projections under the desingularized reduced flow, given by system (3.19). Recall that we defined the return map $\Pi = P \circ \Pi^+ \circ P \circ \Pi^-$ from $N^- \subset P(L^+)$ back to $P(L^+)$. It is now convenient to introduce the additional map $\tilde{\Pi} = P \circ \Pi^+ \circ P : L^- \rightarrow P(L^+)$, which maps points on the lower fold curve back to the silent phase.

Classical case ($\tau_h = 1, \tau_n = 1$)

We distinguish between two different scenarios. For $I < I_c$, there exist two singularities, a folded saddle and a stable node singularity. The unique canard, formed by the stable manifold of the folded saddle singularity, is a separatrix for the basin of attraction of the node singularity. In particular, there

exists a subset of initial conditions $\tilde{N}^- \subset P(L^+)$ within the physiologically relevant domain $0 < h < 1$ that lies in the basin of attraction of the node equilibrium, as well as its complementary subset $(\tilde{N}^-)^c \subset P(L^+)$ relative to this domain. All trajectories within the complementary subset will reach the fold curve L^- in finite time. In theory, this system may be either excitable or oscillatory, depending on the initial conditions. Suppose that we show

$$\Pi((\tilde{N}^-)^c) \subset \tilde{N}^- \tag{4.22}$$

for the return map Π as described in Sect. 3.2. If so, then no singular periodic orbit can exist. In this case, the cell is purely excitable and all trajectories approach the stable node equilibrium, possibly after a transient featuring excursions to the active phase. Since the stable manifold of the folded saddle forms a boundary of the basin of attraction of the node, as long as the h -coordinate h_{fs} of the folded saddle is less than one, it follows that to establish (4.22), it is in fact sufficient to establish that

$$\tilde{\Pi}((L^-)_{fs+}) \subset \tilde{N}^-, \tag{4.23}$$

where $(L^-)_{fs+}$ is the segment of L^- on which $h_{fs} \leq h \leq 1$.

Figure 17 shows an example of this excitable scenario with $I = 3.5$. We will show many plots of this type in the following exposition. The plot on the upper left in Fig. 17 shows the lower fold L^- (red solid) and its projection $P(L^-)$ onto S_a^+ (red dashed), the upper fold L^+ (black solid) and its projection $P(L^+)$ onto S_a^- (black dashed), the two equilibrium points on L^- (the blue circle is a node, the red triangle is a folded saddle, as in the earlier phase plane figures), the canard trajectory formed by a branch of the stable manifold of the folded saddle (green solid), the projection of the canard to the active phase (green dashed), the reduced flow from the projection point in the active phase (cyan solid) up to its intersection with the upper fold, the projection of the intersection point back to the silent phase (cyan dashed), and the reduced flow from the projection point back to the neighborhood of the fold (blue solid). Similar trajectories from projection of the point on L^- with $h = 1$ are also shown.

Both upper panels of Fig. 17 illustrate that $\tilde{\Pi}$ maps the endpoints of $(L^-)_{fs+}$ into \tilde{N}^- . Since orientation is preserved under Π (and $\tilde{\Pi}$ similarly), this finding establishes that condition (4.23) holds, which in turn implies that the set $(\tilde{N}^-)^c$ satisfies condition (4.22), such that the cell is excitable. It is interesting to note the strong contraction, including that resulting from the flow in the active phase, which yields strong compression in h , from the projection back to the silent phase, which gives strong compression in v , and from the ensuing flow there, which contracts strongly in h . The lower panel of Fig. 17 shows the embedding of the two-dimensional plot into \mathbb{R}^3 , using Eq. (2.14).

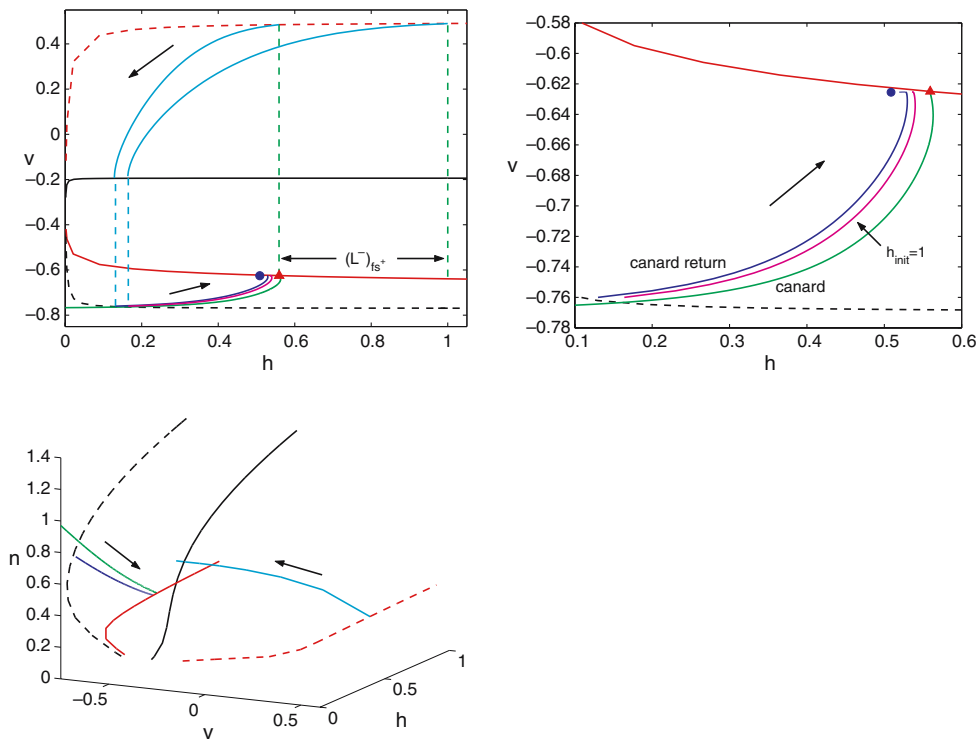


Fig. 17 *Upper left* The return map $\tilde{\Pi}$ generated by the reduced flow for $\tau_h = 1$, $\tau_n = 1$, and $I = 3.5 < I_r < I_c$. Note that the folded singularity is a folded saddle (the corresponding canard is shown in green) and that the black arrows illustrate the direction of the flow. Other objects are explained in the text. *Upper right*: Zoomed view of the silent phase showing the canard as well as the trajectories generated from following both the initial point on L^- satisfying $h = 1$ (magenta, $h_{\text{init}} = 1$) and

the folded saddle point itself (blue trajectory), under $\tilde{\Pi}$. Observe that both trajectories are to the left of the canard and converge to the node, which lies near, but just off, the (red) fold curve L^- . *Bottom* Same fold curves and projections from the upper left plot, as well as the canard (green), the active phase flow of the projected folded saddle (cyan), and its return image in the silent phase (blue), all embedded into \mathbb{R}^3 using Eq. (2.14)

Alternatively, if there exists a subset $N^- \subseteq (\tilde{N}^-)^c$ of the complimentary set such that

$$\Pi(N^-) \subset N^-, \tag{4.24}$$

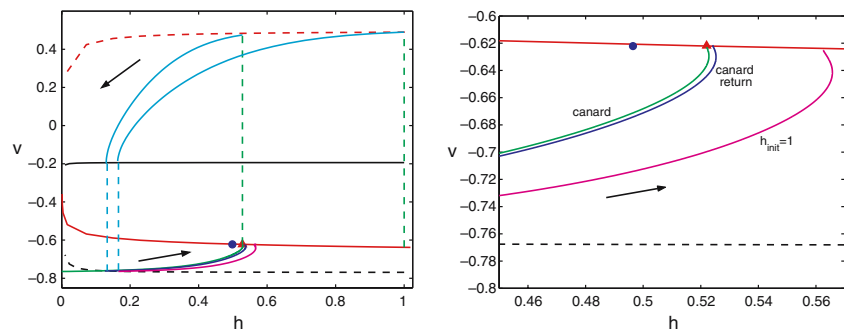
then this will guarantee the existence of a singular periodic orbit by Brouwer’s fixed point theorem or the contraction mapping principle. In particular, if we can show that the boundary point given by the folded saddle is mapped under $\tilde{\Pi}$ to the right of the canard, then it follows immediately that there exists a singular periodic orbit. For example, in Fig. 18 we can show that this singular trajectory is mapped to the right of the canard for $I = 4.1$, which shows the existence of a singular periodic orbit. Therefore, we have (at least) two local singular attractors, the node and a singular periodic orbit, for all I between $I = I_r \approx 4.1$ and $I = I_c$.

Remark 10 Note that the value $I_r \approx 4.1$ is close to the onset of relaxation oscillations observed numerically in system (2.16) with $\tau_h = \tau_n = 1$, which corresponds to a saddle-node bifurcation of periodic orbits in the full system (2.16) with I as the bifurcation parameter.

By continuation it follows that there exist I values within $3.5 < I < 4.1$ such that the initial condition corresponding to the canard trajectory is mapped into the domain of attraction of the node, while the initial condition $h = 1$ is mapped to the right of the canard. The range of I values for which this happens is quite small (a subset of $3.8 < I < 4.1$), as would be expected from the strong contraction observed in Fig. 17. Such a configuration neither rules out nor guarantees the existence of a singular periodic orbit.

For $I = I_r \approx 4.1$, the initial value of the canard will project onto itself and therefore the image of the folded singularity will itself form a singular periodic orbit. In general, corresponding special orbits, known as canard cycles, will exist for system (2.16) and mark the transition from excitable to oscillatory states. The existence of these special orbits is well known in the classical case of the HH model (Rinzel and Miller 1980; Guckenheimer and Oliva 2002). These canard cycles are unstable periodic orbits, co-exist with a stable relaxation orbit and are very sensitive to variation of the parameter I . Multiple unstable canard cycles with varying amplitudes exist for certain values of I (Rinzel and Miller 1980; Guckenheimer and Oliva 2002) and chaotic

Fig. 18 The return map $\tilde{\Pi}$ generated by the reduced flow for $\tau_h = 1$, $\tau_n = 1$, and $I = 4.1$. *Left* all components of the map for the canard and for the $h = 1$ point from L^- are shown. *Right* Zoomed view, showing that both trajectories hit the fold L^- to the right of the folded saddle (red triangle)



behaviour of the system is also expected due to these canard cycles (Guckenheimer and Oliva 2002). For more details we refer to (Rinzel and Miller 1980; Guckenheimer and Oliva 2002).

For applied current $I > I_c$, Proposition 2 implies that there exists a folded node singularity. The cell is in an oscillatory regime since no ordinary singularity exists on the attracting branches S_a^\pm . The main question to resolve is whether or not the cell can support MMO's. Following Sect. 3.3, we have to calculate the return map Π of an arbitrary initial condition in the domain of attraction of the folded node (the funnel). If this trajectory is mapped back into the funnel of the folded node, then the existence of a singular periodic orbit of MMO type follows immediately from the contraction mapping principle. On the other hand, if this initial condition is mapped to the right of the strong canard (outside the funnel) then the existence of a (classical) singular periodic orbit follows. Again, this is a consequence of Proposition 3, which preserves orientation of trajectories under the map Π , and Brouwer's fixed point theorem or the contraction mapping principle.

Note that the branch in S_a^- of the strong eigenvector of the folded node approaches the folded node with positive slope. Hence, the funnel lies to the left of the canard, between the canard and the fold curve L^- . We find that the singular trajectory emanating from the folded node returns to the right of the canard for all $I > I_c$, and the system therefore is in the classical relaxation oscillation regime for $I > I_c$. An example of the return map is shown in Fig. 19 for $I = 5.5 > I_c$. This result is consistent with the fact that the cell enters the classical relaxation regime, with the return of the canard trajectory to the right of the canard itself, for $I_r < I < I_c$ with $I_r \approx 4.1$, as discussed above.

Proposition 4 *In the classical case ($\tau_h = 1$, $\tau_n = 1$), system (2.16) possesses a singular periodic orbit Γ for applied current $I > I_r$. The singular periodic orbit Γ fulfills Assumption 3 for any applied current $I > I_r$. Therefore, no MMO's are expected in this system.*

Despite the non-existence of MMO's in the classical case, we can still observe the effect of the folded node in transients,

when we choose initial conditions that lie in its funnel. An example of this appears in Fig. 20 and it shows clearly the existence of the folded node through the long delay and the observed subthreshold oscillations before the first action potential is fired. This is remarkable since that shows that the squid giant axon has a hidden canard.

Case ($\tau_h > 1$, $\tau_n = 1$)

Recall that the bifurcation diagram for system (3.19) in the silent phase remains relatively invariant as τ_h is increased from 1, with τ_n fixed (Fig. 8). We shall see, however, that increasing τ_h does significantly impact the dynamics in the singular limit, at least for a range of I values.

For $\tau_h > 1$, we again distinguish between the two scenarios, $I < I_c$ and $I > I_c$. For $I < I_c$, there exist a folded saddle and a stable node singularity, the latter of which is independent of τ_h and τ_n . As in the case of $\tau_h = 1$, the unique canard corresponding to the folded saddle singularity is a separatrix for the domain of attraction of the node singularity. Again, we denote by $\tilde{N}^- \subset P(L^+)$ the subset of initial conditions in the domain of attraction of the node equilibrium and by $(\tilde{N}^-)^c$ its complement within the physiologically relevant domain $0 < h < 1$. If Π satisfies (4.22), then the cell is excitable, whereas if (4.24) holds, then the cell is oscillatory, with a singular periodic orbit. For $\tau_h = 1$, the transition from excitable to oscillatory occurs for $I > I_r \approx 4.0$. As $\tau_h > 1$ increases, the I value $I_{r,h}$ at which the transition occurs increases as well. For example, for $\tau_h = 3$, $\tau_n = 1$, and $I = 4$, Fig. 21 shows that $\tilde{\Pi}$ is defined on all of $(L^-)_{f_{s^+}}$, since it is defined on the endpoints of $(L^-)_{f_{s^+}}$ and the flow is orientation preserving, and that (4.22) holds, such that the cell is still excitable. Thus, for fixed $I < I_c$, increasing τ_h alters the global return mechanism and therefore switches the cell from an oscillatory to an excitable state. In fact, $I_{r,h}$ approaches I_c as τ_h approaches $\tau_h^e \approx 1.3$. For $\tau_h > \tau_h^e$, there is no transition, and the cell remains excitable for all $I < I_c$.

This change in excitability has a dramatic influence on the cell in the case $I > I_c$, where the folded saddle bifurcates to a folded node. As for $\tau_h = 1$, the singular funnel of the folded node lies to the left of the strong canard in this parameter

Fig. 19 The image of the folded node under $\tilde{\Pi}$ lies to the right of the canard in the classical case ($\tau_h = \tau_n = 1$) for $I > I_c$. *Left* usual diagram for $I = 5.5$. *Right* embedding of this diagram into \mathbb{R}^3

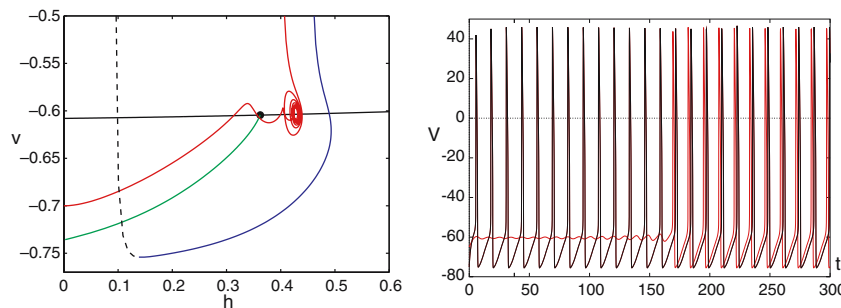
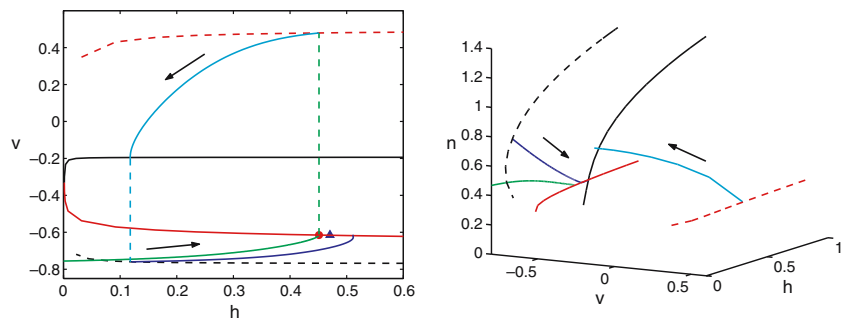


Fig. 20 Transient effects of the folded node for the classical case ($\tau_h = \tau_n = 1$) with $I = 8 > I_c$. *Left* Zoomed image of the fold L^- (black), the folded node (black circle), the strong canard (green), and the projection of a trajectory generated by the three-dimensional flow from system (2.16). Differential coloring is used to highlight qualitatively different components of this trajectory. First, from the initial condition $(h, v) = (0, -0.7)$ in the funnel of the folded node, this trajectory spends significant time in the vicinity of the folded node before

exiting the silent phase (red) and firing an action potential. After the action potential is fired the trajectory returns to the silent phase (black dashed). The return occurs outside of the funnel of the folded node and hence the trajectory is attracted to the classical periodic orbit or relaxation oscillation (blue), which subsequently yields tonic firing. *Right* The v time courses corresponding to the trajectory in the left image (red) as well as that generated by an initial condition outside of the funnel (black)

regime, because the branch in S_a^- of the strong eigenvector of the folded node approaches the folded node with positive slope. For a range of I values, $I_c < I < I_{r,h}$, the return map Π maps initial conditions of the singular funnel of the folded node back into the singular funnel. Therefore, for $\tau_h > \tau_h^e$ and $I_c < I < I_{r,h}$, Assumption 5 is fulfilled for the corresponding singular periodic orbit Γ and we expect MMO's by Theorem 3. Figure 22 shows an example of the projection of the reduced flow for $\tau_h = 3, \tau_n = 1$, and $I = 8$, for which MMO's occur, as well as the resulting MMO.

For each τ_h , for $I > I_{r,h}$, the return map Π maps the strong canard corresponding to the folded node to the right of the canard. This again shows the existence of a singular periodic orbit, but we now expect ordinary relaxation oscillations by Theorem 2. In the case of $\tau_h = 3$, we find $I_{r,h} \approx 9.7$. Figure 23 shows the projection of the reduced flow for $\tau_h = 3, \tau_n = 1$ and $I = 12$. The singular strong canard corresponding to the folded node is mapped to the right of the funnel, so that only relaxation oscillations occur.

Proposition 5 System (2.16) with fixed parameters $\tau_h > \tau_h^e$ and $\tau_n = 1$, where $\tau_h^e \approx 1.3$, possesses a singular periodic orbit Γ for each applied current $I > I_c$. The singular periodic orbit Γ fulfills Assumption 5 for $I_c < I < I_{r,h}$ and

Assumption 3 for $I > I_{r,h}$. Therefore, a transition from an excitable state to MMO's to an oscillatory state is expected as the applied current I is increased.

Remark 11 Similarly to the transition from excitable to oscillatory in the classical case, there exists a value of I close to $I_{r,h}$, where the initial condition of the strong canard corresponding to the folded node is mapped onto the canard itself. This limiting case of a singular periodic orbit fulfilling Assumption 5 is described in Theorem 4 and explains why we can find all kinds of MMO patterns near the transition to classical relaxation oscillations, as shown in Fig. 28 in Sect. 4.4 below.

Case ($\tau_h = 1, \tau_n > 1$)

Unlike the previous cases, we do not consider $I < I_c$ and $I > I_c$ separately in our presentation for $\tau_h = 1, \tau_n > 1$. Instead, recall from Section 4.1 that we distinguish between two subcases, $\tau_n < \tau_n^c$ and $\tau_n > \tau_n^c$, where $\tau_n^c \approx 4.75$ corresponds to the critical value of τ_n where we observe a (degenerate) pitchfork bifurcation at $I = I_c$, as shown in Fig. 9. We shall see that the case of $1 < \tau_n < \tau_n^c$ is qualitatively quite

Fig. 21 The return map $\tilde{\Pi}$ generated by the reduced flow for $\tau_h = 3, \tau_n = 1, I = 4$. Note that the return images of both the folded saddle and the point on L^- with $h = 1$ lie to the left of the canard, in the basin of attraction of the node

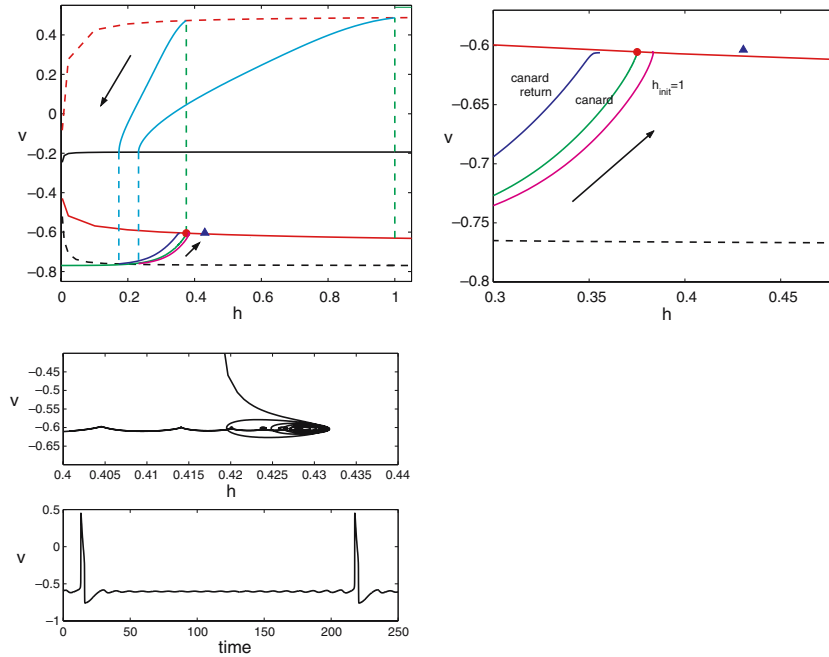
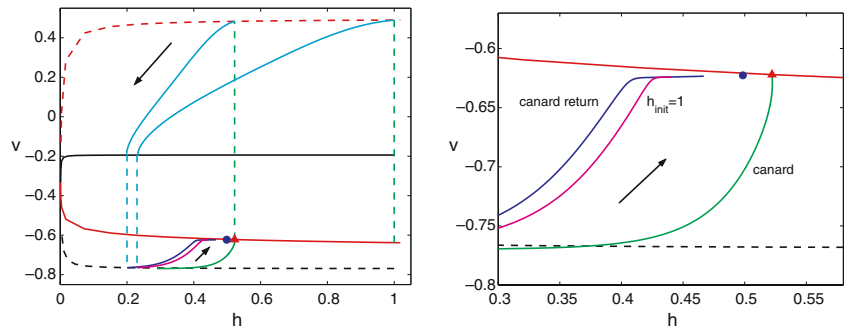


Fig. 22 MMO's occur for $\tau_h = 3, \tau_n = 1, I = 8 > I_c$. *Upper plots* The trajectory generated by following the folded node (canard return) returns into the singular funnel, to the left of the canard itself (green curve) and below L^- (red solid curve), while that generated by following the point on L^- with $h = 1$ ($h_{init} = 1$) does not. *Bottom* The top

panel shows the projection of the trajectory of the three-dimensional flow (2.16) in the vicinity of the folded node. The bottom panel shows the time course of v along the resulting 1^{19} MMO. This MMO is classified as 1^{19} , because 19 subthreshold oscillations occur for each jump to the active phase

similar to the case of $\tau_h > 1, \tau_n = 1$. For $1 < \tau_n < \tau_n^c$, there exist three physiologically relevant singularities, two folded saddles and a node. The basin of attraction of the node is bounded by the two strong canards corresponding to the folded saddles. Figure 24 illustrates the case of $\tau_n = 3$, with $I = 3.5$ and $I = 4.5$. Similarly to the classical case, the folded saddle to the right of the node (i.e., at larger h) is itself moving to the left, closer to the node, as I increases. When τ_n is not too large, there is a transition to relaxation oscillations, with Π mapping the initial conditions corresponding to the strong canards of both folded saddles outside of the basin of attraction of the node (i.e., to the right of the strong canard of the rightmost folded saddle), as I is increased toward I_c . We denote the transitional value by $I_{r,n}$. In the case $\tau_n = 3, I_{r,n}$

is between $I = 3.5$ and $I = 4.5$, as can be seen in Fig. 24. $I_{r,n}$ increases with τ_n , but is always less than I_c for $\tau_n < \tau_n^c$. Now, since $\tau_n < \tau_n^c$, an exchange of stability occurs at $I = I_c$, such that for $I_c < I < I_{SN}^+$, there are a folded node and a regular saddle, with the folded node lying to the left of (i.e., at smaller h values than) the saddle, in addition to the folded saddle at small h . See Fig. 25 for an example. Note that as I increases through I_c , the folded singularity passes through the regular singularity and hence moves across the h -nullcline ($H = 0$). Hence, the slope of the branch in S_a^- of the eigenvector of the folded singularity to which the canard trajectory is tangent switches from negative to positive. Thus, the funnel of the folded node that emerges for $I > I_c$ lies to the left of the canard.

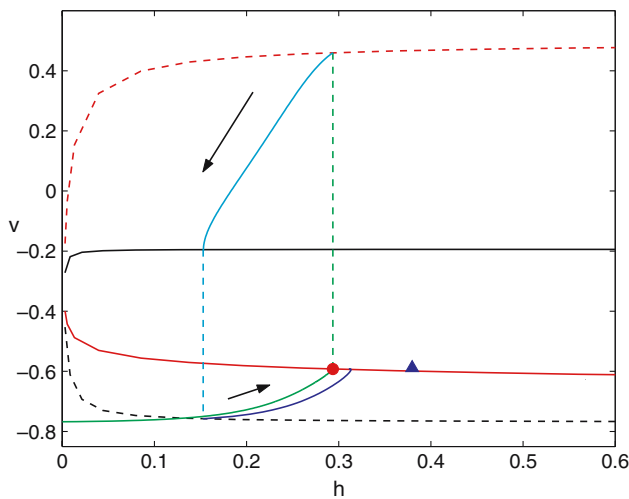


Fig. 23 Projection of the reduced flow for $\tau_h = 3, \tau_n = 1, I = 12$. The folded node returns back to the right of the strong canard (green), whereas the singular funnel is to the left of the strong canard, and hence relaxation oscillations result

For $\tau_n < \tau_n^c$, the transition from excitable to oscillatory occurs already for $I = I_{r,n} < I_c$. For $I_c < I < I_{SN}^+$, the return map applied to an initial condition corresponding to the funnel of the folded node lies outside of the funnel, i.e., to the right of the canard, and thus outside of the basin of attraction of the folded node (Fig. 25). Hence, a singular periodic orbit exists that fulfills Assumption 3 and relaxation oscillations will occur, without MMO's. As I increases toward I_{SN}^+ , the folded saddle and the folded node approach each other (at small h values). These folded singularities annihilate each other in a true folded saddle-node bifurcation at I_{SN}^+ , but this has no influence on the existence of the singular periodic orbit and relaxation oscillations are expected for $I \geq I_{SN}^+$ as well. In summary, for $\tau_n < \tau_n^c$, the passage of I through I_c has little qualitative effect on the dynamics of the system.

Proposition 6 System (2.16) with fixed parameters $\tau_h = 1$ and $\tau_n < \tau_n^c$, where $\tau_n^c \approx 4.75$, possesses a singular periodic orbit Γ for applied current $I > I_{r,n}$. The singular periodic orbit Γ fulfills Assumption 3 for any $I > I_{r,n}$. Therefore, MMO's are not expected and system (2.16) undergoes a direct transition from an excitable to an oscillatory state as I increases through $I_{r,n}$.

Next, we consider the subcase $\tau_n > \tau_n^c$. The bifurcation structure that arises as I increases is opposite to that observed for $\tau_n < \tau_n^c$, in that the folded saddle to the left of the node (i.e., at smaller h) moves to the right, toward the node, with increasing I . There exists a folded saddle to the right of the node as well as the one to the left for some τ_n for I such that $I_{SN}^- < I < I_c$, but for τ_n sufficiently large that $I_{SN}^- > I_c$, this is no longer the case (see Fig. 14). When the rightmost

folded saddle exists, the basin of attraction of the node, for $I < I_c$, is bounded by the stable manifolds of the two saddles; otherwise, it is bounded only by the stable manifold of the left saddle, which always exists.

As in the previous cases, there is again an exchange of stability as I passes through I_c . For $\tau_n > \tau_n^c$, however, as I is increased, the left folded saddle moves to the right and bifurcates to a folded node, which is to the right of the regular saddle. Furthermore, due to the passage of the folded singularity to the opposite side of the h -nullcline, the strong eigenvector of the reduced flow at the folded node switches from positive slope to negative slope at I_c . Thus, the funnel lies in the region to the right of the canard, bounded above by L^- and to the right by the stable manifold of the remaining folded saddle, which lies at larger h than the folded node.

In the subcase $\tau_n^c < \tau_n < \tau_n^e$, Π maps for any $I > I_c$ the initial condition corresponding to the strong canard of the folded node to the left of the folded node (outside the funnel). Therefore a singular periodic orbit exists which fulfills Assumption 3 and relaxation oscillations are expected. This is consistent with the observation that such a singular periodic orbit already exists for $I_{r,n} < I < I_c$.

In the subcase $\tau_n > \tau_n^e$, there exists a range of I values, $I_c < I < I_{r,n}$, for which Π maps the initial condition corresponding to the strong canard of the folded node into the funnel of the folded node (to the right). Hence a singular periodic orbit exists which fulfills Assumption 5 and MMO's are expected. An example of the application of the return map $\tilde{\Pi}$ for this scenario appears in Fig. 26 (left).

As I is increased further, it passes through $I_{r,n}$ and the return map takes the folded node outside of the singular funnel, as shown in Fig. 26 (right). In this case, a singular periodic orbit exists that fulfills Assumption 3, and classical relaxation oscillations are expected. Note that as I increases further through I_{SN}^+ , the folded saddle and folded node annihilate, but this does not affect the existence of relaxation oscillations. Finally, if τ_n is sufficiently large, then there is no saddle node bifurcation of folded singularities (see Fig. 14). Hence, the folded node persists for all I , but the same transition from MMO's (for $I_c < I < I_{r,n}$) to relaxation oscillations (for $I > I_{r,n}$) occurs.

Proposition 7 Fix $\tau_h = 1$ and $\tau_n > \tau_n^c$. There exists a value $\tau_n^e \approx 4.83$ such that if $\tau_n^c < \tau_n < \tau_n^e$, then system (2.16) possesses a singular periodic orbit Γ for applied current $I > I_{r,n}$ with $I_{r,n} < I_c$, and Γ fulfills Assumption 3 for any $I > I_{r,n}$. Thus, a direct transition from the excitable state to an oscillatory state, without MMO's, is expected as the applied current I is increased. Alternatively, if $\tau_n > \tau_n^e$, then (2.16) possesses a singular periodic orbit Γ for applied current $I > I_c$. In this case, the singular periodic orbit Γ fulfills Assumption 5 for $I_c < I < I_{r,n}$ and Assumption 3 for

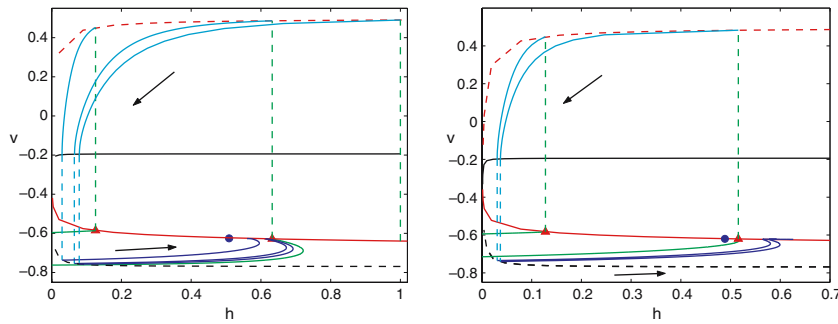


Fig. 24 Examples of return map Π for $\tau_h = 1$, $\tau_n = 3$: $I = 3.5$ (excitable) and $I = 4.5$ (oscillatory). Note that for $I = 3.5$, both canards map into the basin of attraction of the node, as does the point on L^- with $h = 1$. Together, these findings show that Π maps both \tilde{N}^- and $(\tilde{N}^-)^c$

into \tilde{N}^- , and excitability results. For $I = 4.5$, both canards map outside of the basin of attraction of the node. Thus, $\Pi(\tilde{N}^-) \subset (\tilde{N}^-)^c$, and relaxation oscillations result

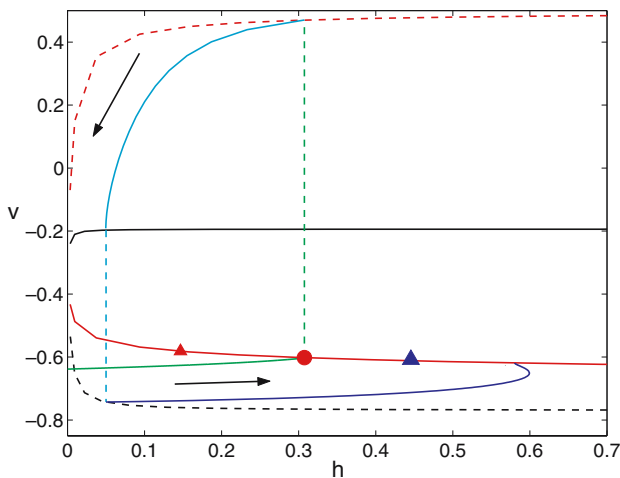


Fig. 25 The return map generated by the reduced flow for $\tau_h = 1$, $\tau_n = 3$, $I = 7 \in (I_c, I_{SN}^+)$. This figure follows the usual notation conventions introduced previously. The return trajectory from the folded node lies outside of the funnel that forms the basin of attraction of the folded node, which is to the left of strong canard of the folded node (note the positive slope with which the strong canard, shown in solid green, approaches the folded node)

$I > I_{r,n}$. Therefore, a transition from an excitable state to MMO's to an oscillatory state is expected as I is increased.

We conclude this section with a final point of discussion, the importance of which was already established in our analysis of the case of $\tau_n > \tau_n^c$. For all values of τ_h and τ_n , as I increases through I_c , there is an exchange of stability between a folded singularity and a regular singularity. As noted above, these singularities meet when $F_v = H = 0$ at the same point, and in the associated stability exchange, the folded singularity moves across the h -nullcline. When a folded singularity lies to the right of the h -nullcline, any associated canards approach the singularity with $\dot{h} < 0$. If a canard does not cross the h -nullcline in backward time and return toward small h values, then all of $P(L^+)$ lies to the

left of the canard, such that the canard does not constrain any basins of attraction. This is the reason, for example, that the rightmost saddle does not impact the dynamics for $\tau_n > \tau_n^c$ with $I < I_c$.

In the classical case, when the folded singularity is to the right of the h -nullcline, it is a folded saddle. For sufficiently small I , the associated canard does not cross the h -nullcline. Hence, condition (4.22) must hold and the system must be excitable. However, the canard does intersect the h -nullcline for all $I > I_h \approx 1.1$, a fairly small value, and relaxation oscillations are no longer ruled out. When the folded saddle becomes a folded node, it lies to the left of the h -nullcline, and hence intersections of the canard and the h -nullcline do not play a role in the (non-)existence of MMO's in the classical case. Further, as discussed earlier and shown in Fig. 8, τ_h does not have a big influence on the bifurcation diagram in the silent phase. Indeed, under variation of τ_h , the same qualitative silent phase dynamics persists, although the active phase (global return) changes the structure sufficiently to cause MMO's for $\tau_h > \tau_h^e$.

In contrast, as can be seen in Fig. 9, τ_n has a big influence on the position of the singularities in the silent phase, and that is the main reason why the reduced flow for $\tau_n > 1$ becomes significantly different than for $\tau_h > 1$ or the classical case. In the case $\tau_n < \tau_n^c$, the exchange of stability occurs when a folded saddle moves from the right of the h -nullcline to the left as I increases through I_c . This is qualitatively similar to the classical case. In the case $\tau_n > \tau_n^c$, however, the exchange of stability occurs when a folded saddle moves from the left of the h -nullcline to the right with increasing I . Hence, this is the only case in which the singular funnel lies to the right of the canard. The return map can only map points from L^- into the singular funnel, and create MMO's, if the corresponding canard turns to the left, toward $h = 0$, in backward time. The folded singularity must be sufficiently close to the nullcline for this to happen, and this is only possible for I sufficiently close to I_c , as shown in the following table:

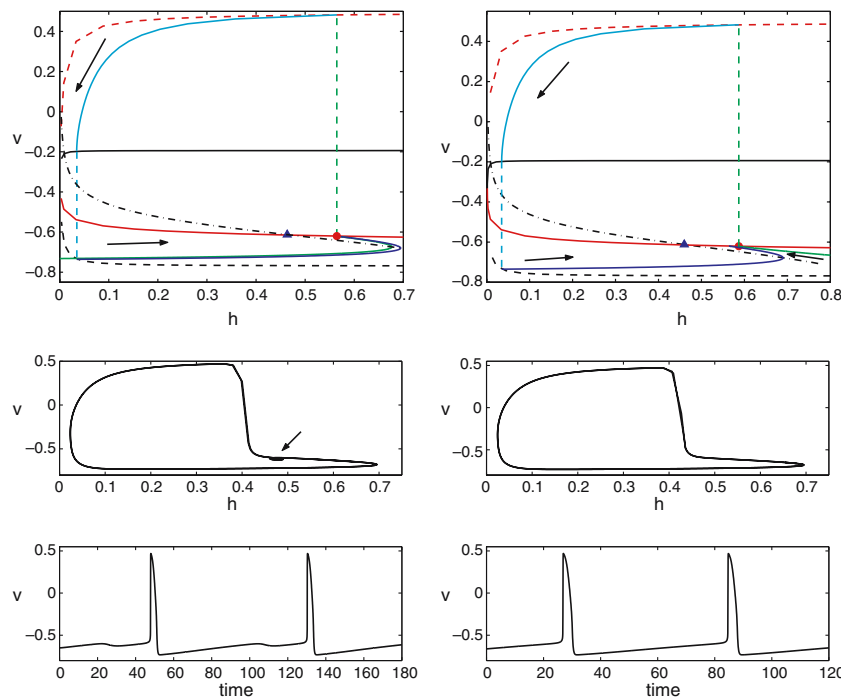


Fig. 26 The return map Π generated by the reduced flow for $\tau_h = 1$, $\tau_n = 7 > \tau_n^c$, and $I = 5.9$ (left top) and $I = 6.1$ (right top), along with the corresponding solutions of the 3-d system (3.18) (bottom). For $I = 5.9$, the return map takes the folded node into the singular funnel, which lies to the right of the folded node (and below L^-), and 1^1 MMO's result (with the subthreshold oscillation labelled by the arrow on the bottom plot). Note that the singular funnel is bounded to the right

by a folded saddle, but this occurs at relatively large h for these parameter values and hence is not visible in this figure. Also observe that while the canard approaches the folded node with negative slope, it does so after crossing the h -nullcline (dash-dotted curve), and in fact the canard tends to small h values in backward time. For $I = 6.1$, the return map takes the folded node to the left of its original location, outside of the singular funnel, and relaxation oscillations result

τ_n	$I_{h \rightarrow 1}$	$I_{h \rightarrow 0}$
6	≥ 5.5	≤ 5.4
7	≥ 6.0	≤ 5.9
8	≥ 6.5	≤ 6.4
9	≥ 7.0	≤ 6.9
10	≥ 7.4	≤ 7.3

Here, the column $I_{h \rightarrow 0}$ refers to I values for which the canard crosses the h -nullcline and intersects $P(L^+)$ with $h < 1$ in backward time, while $I_{h \rightarrow 1}$ refers to I values for which this does not happen. The window of I values where there is a theoretical possibility for MMO's to exist is given by $I_c < I < I_{h \rightarrow 0}$, which is a small range for τ_n near τ_n^e but increases with τ_n . This increase suggests that $I_{r,n}$, at which the onset of relaxation occurs, increases with τ_n , which is consistent with the increase of $I_{r,n}$ with τ_n for $\tau_n < \tau_n^e$ noted earlier. Indeed, for fixed $I > I_c$ but sufficiently close to I_c , there will be a switch from relaxation oscillations to MMO's as τ_n increases. The table, combined with Fig. 9, also shows that $I_{SN}^+ > I_{h \rightarrow 1}$ in all cases for which the saddle-node bifurcation occurs. Hence, MMO's will always be lost below $I = I_{SN}^+$ and the saddle-node bifurcation at $I = I_{SN}^+$ itself will not have an influence on the global dynamics.

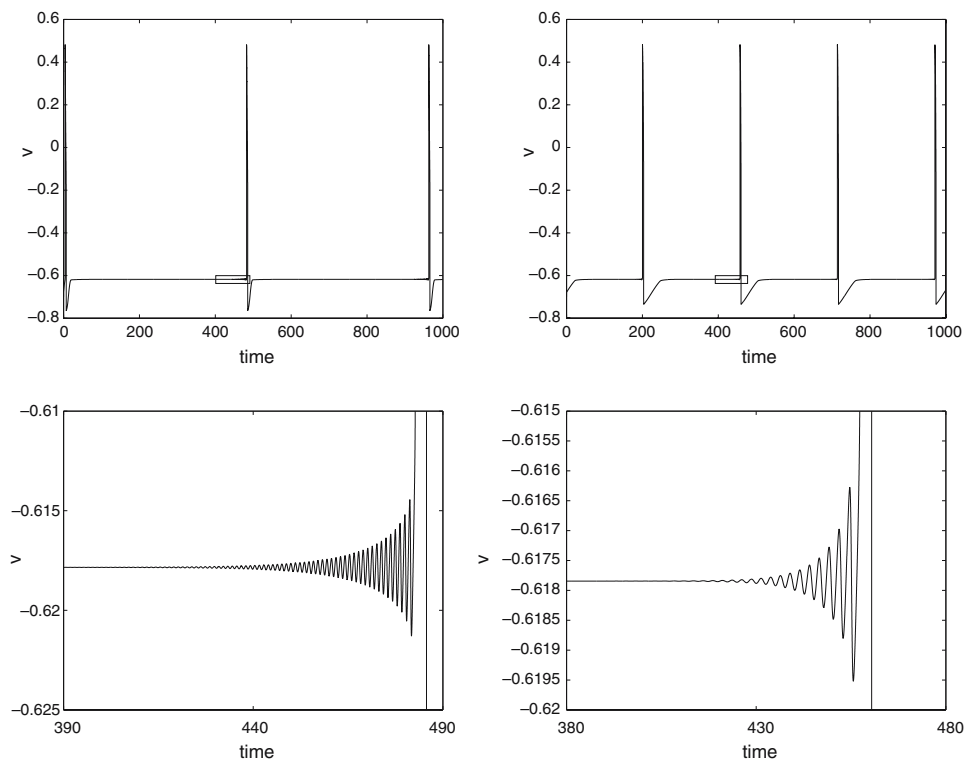
4.4 MMO's

The main observation of the previous section is that if τ_h, τ_n are such that the reduced system remains excitable up to $I = I_c$, then for $I > I_c$ not too large, a singular periodic orbit exists that fulfills Assumption 5, and MMO's are expected (Propositions 4.4 and 4.6).

Case ($\tau_h > \tau_h^e \approx 1.3, \tau_n = 1$)

The theory presented in Sect. 3 predicts MMO's for $I_c < I < I_{r,h}$ and sufficiently small perturbations $\varepsilon \ll 1$. In the case of the 3D HH system (2.16) the value of $\varepsilon \approx 0.008$ is not very small. Therefore the perturbation has a big influence on the system, especially on folded nodes close to the folded saddle-node. In particular, if the corresponding μ value of the folded node is of the order $\mu = O(\sqrt{\varepsilon}) \approx 0.09$ or smaller, then the perturbation ε can be strong enough to push the saddle singularity back to the attracting branch S_a^- , whereby it becomes a node singularity and hence an attractor. Therefore the onset of MMO's can be substantially shifted. For example, in the case ($\tau_h = 3, \tau_n = 1$), we see the onset of MMO's around $I \approx 7.8$ although the singular limit value is $I_c \approx 4.8$. The μ value of the corresponding folded node for

Fig. 27 MMO's for $I = 4.9$ and $\varepsilon = 10^{-4}$ in the case $\tau_h = 3, \tau_n = 1$ (left) and $\tau_h = 1, \tau_n = 7$ (right). Lower figures are zooms of the rectangular areas of corresponding upper figures



$I = 7.8$ is given by $\mu \approx 0.02$, which clearly explains why the onset of MMO's is significantly shifted since the folded node has a very small μ value compared to the perturbation ε . If we make the perturbation ε (artificially) smaller in system (2.16), then the onset of MMO's should be observed closer to the singular limit value of $I_c \approx 4.8$. Indeed, we observe the onset of MMO's in the case ($\tau_h = 3, \tau_n = 1$) already for $I \approx 4.9$ if we set $\varepsilon = 0.0001$ instead of $\varepsilon = 0.008$, as shown in Fig. 27.

This dependence on the singular perturbation parameter ε for the onset of MMO's can also be explained as follows: The singular limit predicts the onset of MMO's at $I = I_c$. At I_c we have a FSN type II singularity, which is related (using a blow-up calculation) to the Hopf bifurcation value in system (2.16) shown in classical bifurcation diagrams using the applied current I as the bifurcation parameter. Using XPPAUT (Ermentrout 2002) to calculate the Hopf bifurcation point¹ for system (2.16) away from the singular limit, one obtains $I \approx 7.8$ for ($\tau_h \geq 1, \tau_n = 1$), which coincides with our observation for the onset of MMO's. We decreased ε in (2.16) and repeated the AUTO calculation to find that the Hopf point converges to I_c for $\varepsilon \rightarrow 0$, as expected from our singular perturbation analysis. The following table displays some values from this AUTO calculation:

ε	$I_{Hopf},$ ($\tau_h = 1, \tau_n = 1$)	$I_{Hopf},$ ($\tau_h = 10, \tau_n = 1$)	$I_{Hopf},$ ($\tau_h = 1, \tau_n = 10$)
0.01	8.3	8.4	6.0
0.0083	7.8	7.8	5.9
0.001	5.2	5.2	5.0
0.0001	4.9	4.9	4.9

Therefore, the Hopf bifurcation value I_{Hopf} converges relatively fast to I_c . This confirms our theory nicely and shows that our predictions on the existence of different oscillatory patterns like MMO's are valid as we move away from the singular limit, albeit just qualitatively.

The transition from MMO's to relaxation oscillations occur close to the expected singular value $I = I_{r,h}$ and does not display the same sensitivity to the perturbation ε as the onset of MMO's. The following table shows that the values of I at which this transition occurs remain close to $I = 9.7$, the value predicted in the singular limit, even as ε increases over several orders of magnitude, for $\tau_h = 3, \tau_n = 1$. The global return mechanism is robust under perturbation, so this insensitivity is expected.

ε	$I_{r,h}(\tau_h = 3, \tau_n = 1)$	$I_{r,n}(\tau_h = 1, \tau_n = 7)$
0.01	9.2	6.0
0.0083	9.3	6.0
0.001	9.7	5.9
0.0001	9.7	–

¹ The Hopf bifurcation is always sub-critical.

Fig. 28 Projections from system (2.16) and voltage time courses for four MMO's generated with $\tau_h = 3, \tau_n = 1$. Note that the axis scales are different for different plots. Upper left $I = 9$ yields 2^3 MMO's. Upper right $I = 9.13$ yields $2^1 2^2 2^2$ MMO's. Lower left $I = 9.22$ yields 3^1 MMO's. Lower right $I = 9.254$ yields $3^1 4^1$ MMO's

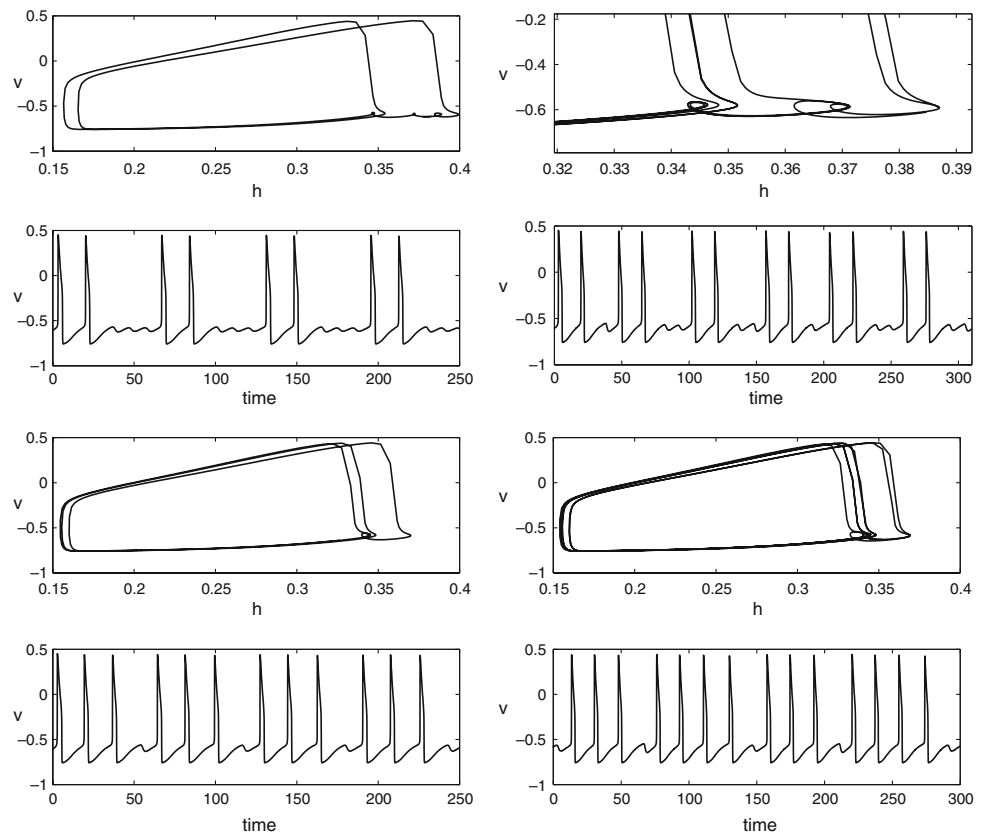


Figure 28 shows examples of MMO's for $\tau_h = 3$, for different values of I . In general, we observe MMO's of the form L^s , where L, s are positive integers such that L increases with I and, for each fixed L, s decreases as I increases. However, we also observe MMO's that are not of the form L^s over the transitions between L^s MMO's. Examples of MMO's of this type appear in the upper and lower right plots in Fig. 28. One can find a wide variety of MMO patterns of the form $1^k 1^m \dots 1^l$. Figure 29 shows the 1^s MMO patterns predicted by our analysis in the singular limit. These were obtained by reducing ε in system (2.16) to 0.001. A complete explanation of the transitions between $1^s, L^s$, and more exotic MMO patterns as ε varies is beyond the scope of this work.

Case ($\tau_n > \tau_n^e \approx 4.8, \tau_h = 1$)

Similarly to the ($\tau_h = 3, \tau_n = 1$) case, MMO's are only observed for $5.7 < I < 6.0$ in the case ($\tau_n = 7, \tau_h = 1$). The μ value of the corresponding folded node for $I = 5.7$ is given by $\mu \approx 0.07$ which again explains why the onset of MMO's is significantly shifted, since the folded node has a small μ value compared to the singular perturbation parameter ε . If we make the perturbation ε (artificially) smaller in system (2.16), then the onset of MMO's should be observed closer to the singular limit value of $I_c \approx 4.8$. Indeed, we observe

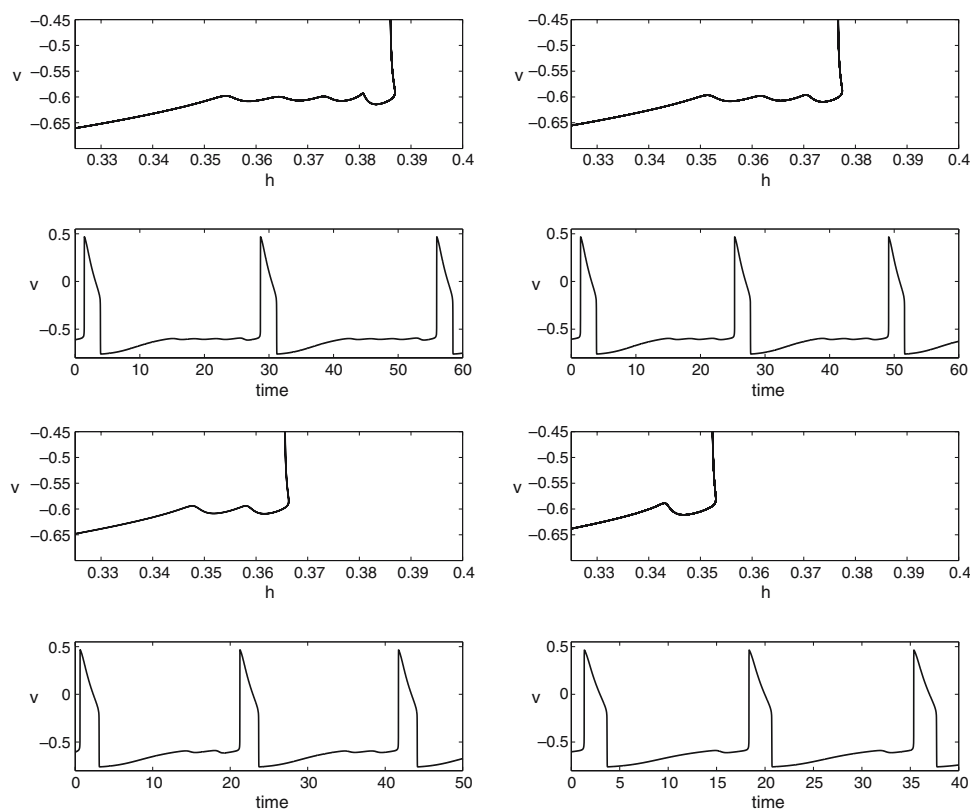
the onset of MMO's in the case ($\tau_h = 1, \tau_n = 7$) already for $I \approx 4.9$ if we set $\varepsilon = 0.0001$ instead of $\varepsilon = 0.008$, as shown in Fig. 27. Figure 30 shows some examples of MMO patterns observed for ($\tau_n = 7, \tau_h = 1$) under variation of I . Over the whole MMO range, the MMO's appear to be the form 1^s , where s decreases as I increases.

As was seen for $\tau_h > 1$, the transition from MMO's to relaxation oscillations for $\tau_n > 1$ is not as sensitive to the perturbation ε as is the onset of MMO's, due to the robustness of the global return mechanism, and occurs close to the expected value $I = I_{r,n} \approx 5.9$ computed in the singular limit. The table above gives values at which the transition to relaxation oscillations occurs for $\tau_h = 1, \tau_n = 7$ for different positive ε values. Note that for $\varepsilon = 0.0001$, we experience some loss of numerical accuracy, and hence no value is given in that case.

5 Discussion

In this paper, we have systematically explored the transitions in activity patterns that emerge as time constants τ_h, τ_n associated with the activation/inactivation variables n, h in the Hodgkin–Huxley equations (1.5) are varied. To do this, we nondimensionalized the system to obtain Eqs. (2.13) and applied a center manifold reduction to obtain system (2.16).

Fig. 29 Projections from system (2.16) and voltage time courses for four MMO's generated with $\tau_h = 3$, $\tau_n = 1$ with ϵ reduced to 0.001. *Upper left* $I = 8.5$ yields 1^4 MMO's. *Upper right* $I = 8.7$ yields 1^3 MMO's. *Lower left* $I = 9.0$ yields 1^2 MMO's. *Lower right* $I = 9.4$ yields 1^1 MMO's



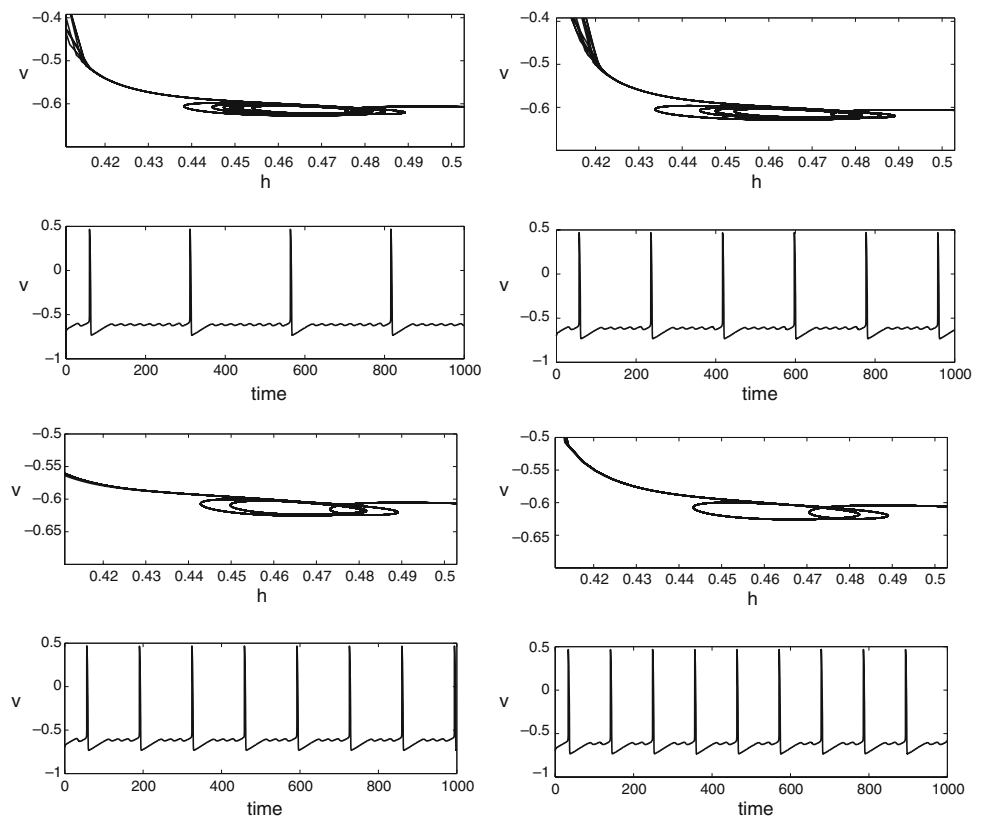
Capitalizing on the decomposition of system (2.16) into one fast and two slow variables, we performed a geometric analysis of the solution structure in the singular limit, using relevant theory from the literature on relaxation oscillations, canards, and MMO's (Szmolyan and Wechselberger 2001, 2004; Wechselberger 2005a; Brøns et al. 2006). This analysis relies heavily on the study of the reduced system (3.18). Although we work with a variety of systems obtained from system (1.5), it is important to note that the results apply to the qualitative behavior of system (1.5) itself, although precise I values at which particular phenomena occur differ between system (1.5) and system (2.16), in accordance with the center manifold reduction described in Theorem 1. For example, system (1.5) with $\tau_h = 3$ and $\tau_m = \tau_n = 1$ exhibits MMOs on approximately the interval $I \in (9.8, 16.2)$, whereas system (2.16) with $\tau_h = 3$ and $\tau_n = 1$ yields MMOs on approximately $I \in (7.8, 9.3)$.

The three key parameters in our analysis are τ_h , τ_n and I . To avoid further lengthening of the work, we focused on the cases $(\tau_h > 1, \tau_n = 1)$ and $(\tau_h = 1, \tau_n > 1)$, in addition to the classical case of $\tau_h = \tau_n = 1$. Within these cases, the main results of the analysis can be summarized very succinctly. For all (τ_h, τ_n) studied, the system is excitable, with an asymptotically stable fixed point corresponding to a quiescent state, for I small. For all parameters other than the unique point $(\tau_h = 1, \tau_n \approx 4.75)$, system (3.18) experiences a transcritical bifurcation at the same fixed value of I ,

namely $I_c \approx 4.83$. The universality of this structure implies that, as I increases through I_c , only two progressions are possible. One possibility is that a transition from the excitable state to the existence of relaxation oscillations will occur for $I < I_c$, and then relaxation oscillations will persist for $I > I_c$. The other possibility is that the system will remain excitable up to $I = I_c$, in which case MMO's arise on some range $I_c < I < I_r$, and relaxation oscillations exist for $I > I_r$. Our analysis shows that if either τ_h or τ_n is increased from 1, then a transition from the former to the latter case will occur. Moreover, the analysis predicts where in parameter space all of these transitions are expected to occur, for ϵ sufficiently small, which gives an approximation to the transition values as ϵ moves away from zero. Based on the universality of the mechanisms underlying these transitions in the HH model, and the weak effect of τ_h on the bifurcation of relevant structures when $\tau_n = 1$ (Fig. 8), we predict that similar results arise when τ_h, τ_n are both increased from 1, albeit with quantitative differences.

The existence of the MMO's that we study here, in the modified HH equations (1.5), was pointed out in several earlier works (Doi and Kumagai 2001, 2005; Doi et al. 2001, 2004). However, the earlier consideration of these solutions was incomplete, in that only isolated parameter values were considered. Moreover, the existence of these solutions was attributed to a one-slow-variable mechanism. Indeed, the analysis in the earlier papers was based on assuming that

Fig. 30 Projections from system (2.16) and voltage time courses for four MMO's generated with $\tau_h = 1, \tau_n = 7$. *Upper left* $I = 5.7$ yields 1^8 MMO's. *Upper right* $I = 5.725$ yields 1^5 MMO's. *Lower left* $I = 5.75$ yields 1^3 MMO's. *Lower right* $I = 5.8$ yields 1^2 MMO's



h was a slow variable and setting $n = n_\infty(v)$ or assuming that n was a slow variable and setting $h = h_\infty(v)$.

Canards in a two-dimensional reduction of the HH model, with one slow variable, have been studied previously (Moehlis 2006). The one-slow-variable approach is problematic for the three-dimensional HH model, however, because as our nondimensionalization demonstrates, (h, n) evolve at comparable speeds and are significantly slower than v . The one-slow-variable treatment for the 3-d model led to a claim that fundamentally different bifurcation structures are responsible for slow oscillatory solutions depending on whether τ_h or τ_n is increased (Doi et al. 2001, 2004; Doi and Kumagai 2005). Our two-slow-variable analysis corrects this claim, showing that in fact the slow solutions are MMO's and that the differences in solution structure relate to the distance of I from I_c , not to differences between the $\tau_h > 1$ and $\tau_n > 1$ cases. We want to emphasize that the same local structure responsible for MMO's, canards of folded node type, exists in the classical case ($\tau_h = \tau_n = 1$) of the HH equations and can be observed in transients as shown in Fig. 20 ('the hidden canard of the squid giant axon'). This observation strongly supports the two-slow-variable approach. The properties of the MMO's explored in our work also depend on μ , the ratio of the eigenvalues of the folded node equilibrium of the desingularized reduced system, and on the image of certain sets under the global return map Π , relative to the funnel of

the folded node, as indicated in our many figures and elaborated within the theory of the generalized canard phenomenon (Wechselberger 2005a; Brøns et al. 2006). In particular, the nature of the subthreshold oscillations associated with the MMO's is determined by precisely these factors.

Note that the onset of oscillations that we observe by studying the desingularized reduced system also corresponds to a bifurcation for the full system (2.16). In past work, Guckenheimer et al. have studied MMO's in the vicinity of codimension-two subcritical Hopf-homoclinic bifurcations in three-dimensional systems (Guckenheimer et al. 1997; Guckenheimer and Willms 2000). In the singular limit, we may indeed obtain an orbit homoclinic to a fixed point on the repelling middle branch S_r of the critical manifold S_0 , providing a theoretical opportunity for the existence of some form of singular Hopf-homoclinic bifurcation. However, blow-up calculations can be done to show that this homoclinic orbit does not persist when ε is made positive. Hence, the relationship of the phenomena that we have analyzed in the HH model to the work in (Guckenheimer et al. 1997; Guckenheimer and Willms 2000) requires further clarification.

Finally, we point out that the canard mechanism studied here also supports the possibility of chaos, which has been studied in the Hodgkin–Huxley equations previously (Rinzel and Miller 1980; Guckenheimer and Oliva 2002) but is beyond the scope of this paper. A further exploration of the

ϵ -dependence of the pattern of large and small oscillations seen in the observed MMO's, along with the development of a general theory that spells out the full range of patterns expected for $\mu = O(\sqrt{\epsilon})$ or smaller, also remains for future work.

Acknowledgments JR was partially supported by National Science Foundation award DMS-0414023. We thank John Guckenheimer for his helpful comments on an earlier version of the manuscript.

References

- Benoit E (1983) Systèmes lents-rapides dans \mathbb{R}^3 et leur canards. *Astérisque* 109-110:159–191
- Brøns M, Krupa M, Wechselberger M (2006) Mixed mode oscillations due to the generalized canard phenomenon. *Fields Inst Commun* 49:39–63
- Doi S, Inoue J, Kumagai S (2004) Chaotic spiking in the Hodgkin Huxley nerve model with slow inactivation of the sodium current. *J Integr Neurosci* 3:207–225
- Doi S, Kumagai S (2001) Nonlinear dynamics of small-scale biophysical neural networks. In: Poznanski R (ed) *Biophysical neural networks: foundations of integrative neuroscience*. Mary Ann Liebert Inc.
- Doi S, Kumagai S (2005) Generation of very slow rhythms and chaos near the Hopf bifurcation in single neuron models. *J Comp Neurosci* 19:325–356
- Doi S, Nabetani S, Kumagai S (2001) Complex nonlinear dynamics of the Hodgkin–Huxley equations. *Biol Cybern* 85:51–64
- Drover J, Rubin J, Su J, Ermentrout B (2004) Analysis of a canard mechanism by which excitatory synaptic coupling can synchronize neurons at low firing frequencies. *SIAM J Appl Math* 65:69–92
- Ermentrout B (2002) *Simulating, analyzing, and animating dynamical systems*. SIAM, Philadelphia
- Fenichel N (1979) Geometric singular perturbation theory. *J Diff Eq* 31:53–98
- FitzHugh R (1960) Thresholds and plateaus in the Hodgkin–Huxley nerve equations. *J Gen Physiol* 43:867–896
- Guckenheimer J, Haiduc R (2005) Canards at folded nodes. *Mosc Math J* 5:91–103
- Guckenheimer J, Harris-Warrick R, Peck J, Willms A (1997) Bifurcation, bursting, and spike frequency adaptation. *J Comp Neurosci* 4:257–277
- Guckenheimer J, Oliva R (2002) Chaos in the Hodgkin–Huxley model. *SIAM J Appl Dyn Sys* 1:105–114
- Guckenheimer J, Wechselberger M, Young L-S (2005) Chaotic attractors of relaxation oscillators. *Nonlinearity* 19:701–720
- Guckenheimer J, Willms A (2000) Asymptotic analysis of subcritical Hopf-homoclinic bifurcation. *Physica D* 139:195–216
- Hodgkin A, Huxley A (1952) A quantitative description of membrane current and its application to conduction and excitation in nerve. *J Physiol (London)* 117:500–544
- Jones C (1995) Geometric singular perturbation theory, in dynamical systems. *Lecture Notes Math* 1609. Springer, Heidelberg, pp 44–120
- Milik A, Szmolyan P, Loeffelmann H, Groeller E (1998) Geometry of mixed-mode oscillations in the 3d autocatalator. *Int J Bif Chaos* 8:505–519
- Moehlis J (2006) Canards for a reduction of the Hodgkin–Huxley equation. *J Math Biol* 52:141–153
- Nagumo J, Arimoto S, Yoshizawa S (1962) An active pulse transmission line simulating nerve axon. *Proc. IRE* 50:2061–2070
- Rinzel J (1985) Excitation dynamics: insights from simplified membrane models. *Fed. Proc.* 44:2944–2946
- Rinzel J, Ermentrout B (1989) Analysis of neural excitability and oscillations. In: Koch C, Segev I (eds) *Methods in neuronal modeling: from synapses to networks*. MIT Press, Cambridge
- Rinzel J, Miller R (1980) Numerical calculation of stable and unstable periodic solutions to the Hodgkin–Huxley equations. *Math Biosci* 49:27–59
- Rubin J (2005) Surprising effects of synaptic excitation. *J Comp Neurosci* 18:333–342
- Szmolyan P, Wechselberger M (2001) Canards in \mathbb{R}^3 . *J Diff Eq* 177:419–453
- Szmolyan P, Wechselberger M (2004) Relaxation oscillations in \mathbb{R}^3 . *J Diff Eq* 200:69–104
- Wechselberger M (2005a) Existence and bifurcation of canards in \mathbb{R}^3 in the case of a folded node. *SIAM J Appl Dyn Sys* 4:101–139
- Wechselberger M (2005b) Poincaré maps for relaxation oscillations in \mathbb{R}^3 - invariant manifolds, canards and turning points. In: *Proceedings of Equadiff 03*, Hasselt, Belgium